AGU PUBLICATIONS

JGR

Journal of Geophysical Research: Planets

RESEARCH ARTICLE
10.1002/2016JE005052

Key Points:
- Valleys and paleolakes in northern Arabia Terra formed during a relatively short event in the Hesperian to middle Amazonian
- Fluvial valleys may represent a late, widespread episode of aqueous activity that was possibly contemporaneous with alluvial fan activity
- Snowmelt hydrology is consistent with a cold, wet, and possibly habitable environment that occurred late in Martian climate history

Supporting Information:
- Supporting Information S1

Correspondence to:
S. A. Wilson,
wilsons@si.edu

Citation:
Wilson, S. A., A. D. Howard, J. M. Moore, and J. A. Grant (2016), A cold-wet middle-latitude environment on Mars during the Hesperian-Amazonian transition: Evidence from northern Arabia valleys and paleolakes, *J. Geophys. Res. Planets*, *121*, 1667–1694, doi:10.1002/2016JE005052.

Received 7 APR 2016
Accepted 9 AUG 2016
Accepted article online 11 AUG 2016
Published online 17 SEP 2016

©2016. American Geophysical Union. All Rights Reserved.

A cold-wet middle-latitude environment on Mars during the Hesperian-Amazonian transition: Evidence from northern Arabia valleys and paleolakes

Sharon A. Wilson[1,2], Alan D. Howard[2], Jeffrey M. Moore[3], and John A. Grant[1]

[1]Center for Earth and Planetary Studies, National Air and Space Museum, Smithsonian Institution, Washington, District of Columbia, USA, [2]Department of Environmental Sciences, University of Virginia, Charlottesville, Virginia, USA, [3]NASA Ames Research Center, Space Sciences Division, Moffett Field, California, USA

Abstract The growing inventory of post-Noachian fluvial valleys may represent a late, widespread episode of aqueous activity on Mars, contrary to the paradigm that fluvial activity largely ceased around the Noachian-Hesperian boundary. Fresh shallow valleys (FSVs) are widespread from ~30 to 45° in both hemispheres with a high concentration in northern Arabia Terra. Valleys in northern Arabia Terra characteristically start abruptly on steeper slopes and terminate in topographic depressions at elevations corresponding to model-predicted lake levels. Longer valley systems flowed into and out of chains of paleolakes. Minimum discharges based on the dimensions of the incised channel assuming medium to coarse sand-size grains ranges from tens to hundreds of $m^3 s^{-1}$, respectively, consistent with formation via snowmelt from surface or sub-ice flows. Hydrologic calculations indicate the valleys likely formed in hundreds of years or less, and crater statistics constrain the timing of fluvial activity to between the Hesperian and middle Amazonian. Several craters with channels extending radially outward supports evidence for overflow of interior crater lakes possibly fed by groundwater. Most FSVs occur away from young impact craters which make an association with impact processes improbable. The widespread occurrence of FSVs along with their similar morphology and shared modest state of degradation is consistent with most forming during a global interval of favorable climate, perhaps contemporaneous with alluvial fan formation in equatorial and midlatitudes. Evidence for a snowmelt-based hydrology and considerable depths of water on the landscape in Arabia supports a cold, wet, and possibly habitable environment late in Martian history.

1. Introduction

Several paradigm shifts have occurred over the past several decades as our understanding of the hydrological and climatologic history of Mars has evolved. It is generally accepted that the early climate on Mars was capable of sustaining an active hydrological cycle and that (possibly episodic) precipitation and runoff formed the low-to-middle latitude belt of valley networks [*Carr*, 2012; *Craddock and Howard*, 2002; *Grant*, 2000; *Howard et al*., 2005; *Hynek and Phillips*, 2001, 2003; *Irwin and Howard*, 2002; *Irwin et al*., 2005a]. Age analyses from crater counts suggest a sudden decline in fluvial activity by the early Hesperian, presumably associated with the loss of the early denser atmosphere [*Fassett and Head*, 2008; *Hynek et al*., 2010; *Fassett and Head*, 2011]. The climate in the Hesperian and Amazonian was generally considered to be less favorable for precipitation (most likely snow) and runoff, with aqueous processes restricted to possible hydrothermal runoff on a few volcanic edifices and occasional outburst floods. This view of a cold, arid post-Noachian Mars is being challenged by a growing inventory of well-preserved midlatitude and equatorial fluvial valleys that are smaller and presumably younger than the classic late Noachian valley networks [e.g., *Adeli et al*., 2016; *Dickson et al*., 2009; *Fassett and Head*, 2008, 2011; *Howard and Moore*, 2011; *Hynek et al*., 2010; *Irwin et al*., 2005a; *Morgan and Head*, 2009; *Salese et al*., 2016; *Warner et al*., 2010a, 2010b].

These "young" valleys are morphologically distinct from both ancient valley networks and gullies [e.g., *Dickson et al*., 2009; *Fassett et al*., 2010; *Hobley et al*., 2014; *Howard and Moore*, 2011]. The Noachian valley networks are deeply incised (50–250+ m), form strongly parallel to dendritic networks, and are heavily degraded. By contrast, gullies [*Malin and Edgett*, 2000] are characterized by well-defined source areas, higher gradients, and are, in general, narrower and shorter in length [*Fassett et al*., 2010] (Figure 1). The "fresh shallow valleys" (FSVs), presented in this study, are defined by their morphology [*Hobley et al*., 2014]. The

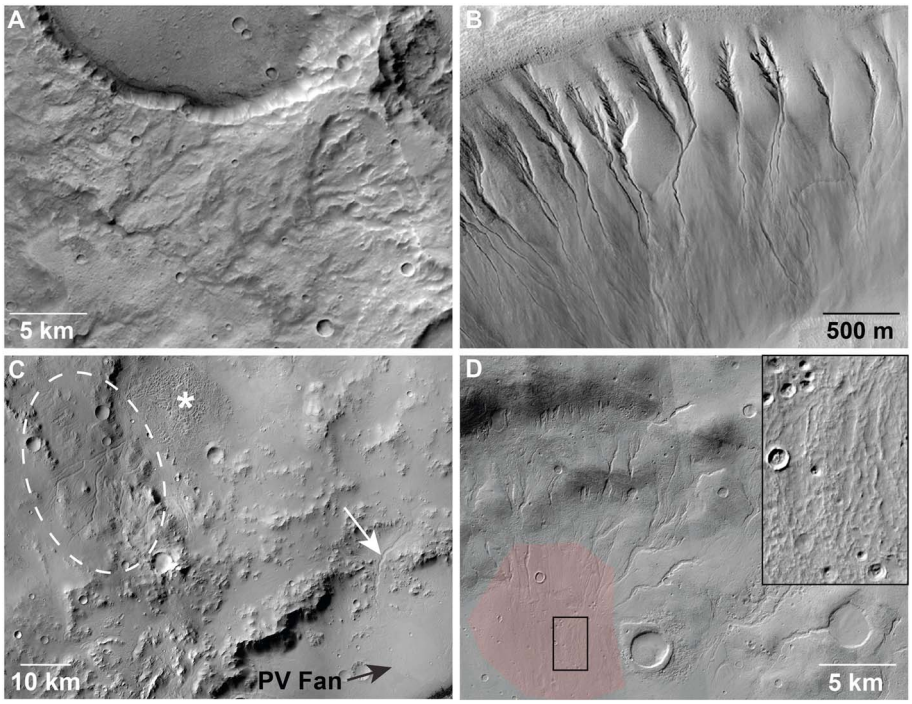

Figure 1. Morphology and characteristics of valleys on Mars. (a) Noachian-Hesperian valley networks in the southern highlands of Mars are generally deeply incised, strongly dendritic, and heavily degraded relative to fresh shallow valleys (FSVs). Example of a dissected outer crater rim near 25°S, 154°E. Subframe of CTX P11_005259_1541 (5.14 m scaled pixel width). (b) Gullies [*Malin and Edgett*, 2000] have well-defined source areas, higher gradients, and are, in general, narrower and shorter in length relative to FSVs. Subframe of HiRISE PSP_003418_1335 (25 cm scaled pixel width) in Noachis Terra near 46°S, 18.8°E. (c) FSVs in the equatorial region commonly form on interior and exterior crater rims, such as Peace Vallis (white arrow) on the northern rim of Gale crater, which terminates in the Peace Vallis (PV) fan (black arrow). FSVs northwest of Gale (white dashed circle) are weakly dendritic, often with constant valley widths and indistinct headwater source, terminating in a fan-shaped deposit (asterisk sign). Subframe of HRSC H5273 centered near 4.2°S, 136.8°E. (d) FSVs are commonly incised into the latitude-dependent mantle, and flat valley floors can be modified ice-related processes [*Moore and Howard*, 2005]. FSVs originating on an interior crater rim of an unnamed crater (near 39.2°S, 19.3°E) terminate in a small fan deposit (shaded red); inset (black box) shows inverted channels on fan surface (modified from *Howard et al.* [2014]). Subframes of CTX B17_016340_1402 (5.14 m scaled pixel width) and P16_007255_1411 (5.09 m scaled pixel width). North to top in all images.

term *fresh* implies the valleys lack significant overall degradation at the resolution of images from the Context Camera (CTX, ~6 m per pixel scale [*Malin et al.*, 2007]) and minimal modification of the valley sidewalls, which is consistent with their inferred post-Noachian age [e.g., *Hobley et al.*, 2014; *Howard and Moore*, 2011]. At a submeter to meter scale, however, FSVs in the midlatitudes are typically modified by mantling material likely related to periglacial processes [*Hobley et al.*, 2014; *Howard and Moore*, 2011]. FSVs are narrow (typically less than 500 m) and *shallow*, generally incising no more than a few decameters into the surrounding terrain.

This investigation uses high-resolution image and topographic data sets to characterize the morphology, occurrence, age, and the possible source(s), magnitudes and frequency of the formative flows responsible for FSV formation in northern Arabia Terra. A regional hydrologic routing model examines flow paths of water across the landscape and estimates the volume and area of filled depressions. Possible correlations between impact processes and valley formation were investigated by analyzing relationships between FSVs and crater ejecta including their association with variables such as crater age, size, latitude, and ejecta elevation and morphology. We address the question of whether the FSVs formed as a result of a multiplicity of local mechanisms occurring as temporally scattered events (e.g., impact related) versus one or more episodes of widespread fluvial activity related to a global interval of favorable climate. This distinction is important, as it provides insight into the geologic and climatic environments that permitted the formation of FSVs in a post-Noachian climate with implications for potential late-stage habitability on Mars.

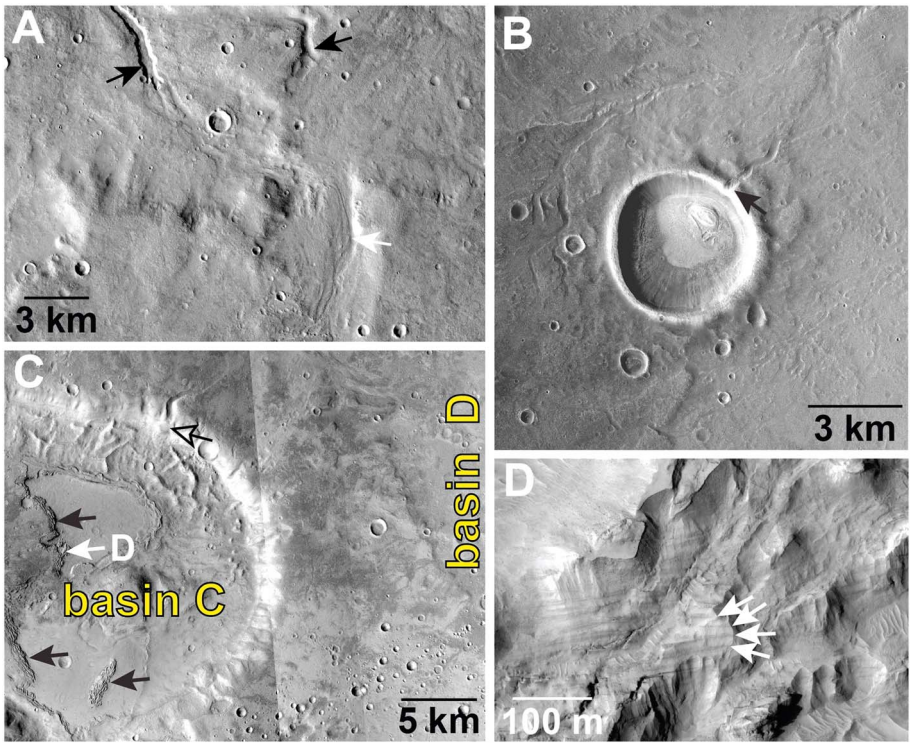

Figure 2. Examples of landforms discussed throughout text; see Figure 4 for regional distribution. (a) *Morphological Types of FSVs* (after *Hobley et al.* [2014]). Type 1 valleys (black arrows) are narrowly incised, and Type 2 valleys (white arrow) are wider, shallower, and sometimes have apparent bedforms (see Figure 4 for context). Subframe of CTX P03_002284_2181 (5.88 m scaled pixel width). (b) *Pollywogs*. "Pollywog" craters have a single channel that extends outward from their rim (black arrow, see Figure 4 for context). Crater is ~4.3 km diameter and is located near 35.0°N, 8.0°E. Subframe of CTX B16_015984_2149 (5.83 m scaled pixel width). (c) *Deltas and basin floor deposits*. Small lobe-shaped deposit (hollow black arrow) on northern interior rim of basin C inferred to be a sedimentary delta (see Figure 7a for context). The FSV and associated delta formed as water overflowed from basin D into basin C (via a small water-filled depression in between). See Table 2 and additional deltas in Figures 10 and 14c–14e. *Basin floor deposits* (black arrows) occur on the lowest elevations of several model-predicted filled basins. The surface of these deposits has troughs oriented roughly parallel to the basin walls. These deposits can also occur as isolated mounds (see bottom black arrow and Figure 8b). White arrow indicates location of Figure 2d. Subframes of CTX images P01_001440_2174, P15_006807_2187, and P17_007809_2169 (~5.9 m scaled pixel width). (d) *Detail of basin floor deposits*. Horizontal layers exposed in scarp of basin floor deposits. Deposit is fine-grained, massive, repetitive packages of ~10 m thick medium-toned layers separated by thinner dark-toned layers. These deposits may consist of ice-rich sediment that was deposited in a standing water environment. Subframe of HiRISE PSP_001440_2175 (29.5 cm scaled pixel width). North to top in all images.

2. Background

2.1. Morphology and Nature of FSVs

Previous studies have identified two morphological types of FSVs [*Hobley et al*., 2014] (Figure 2a). Type 1 valleys are narrow, sinuous, and entrenched valleys typically with sharp upper edges at scale of CTX images. They are generally "V" to slightly "U shaped" with widths of 20–50 + m and may range from a few hundred meters to several kilometers in length [*Hobley et al*., 2014]. Type 1 valleys are often unbranched, start and terminate abruptly by narrowing and shallowing, and may lack obvious fluvial features upstream or downstream. Along relatively straight reaches, FSVs exhibit relatively constant widths and depths. Several Type 1 valleys may chain together and can be connected to (or interspersed with) Type 2 valleys. Type 2 valleys are generally wider with near-parallel borders and nearly flat floors that sometimes exhibit low longitudinal lineations that could be bedforms. These apparent bedforms, analogous to fluvial bars, low banks, or braiding, could have formed as a result of migrating flows within the floodplain (Figures 2a and 9b).

FSVs can be locally integrated into dendritic patterns but are usually not space-filling networks. Individual FSVs often occur as scattered, isolated valleys or sparsely branched networks with individual valleys generally not extending more than a few tens of kilometers (Figures 1 and 2). They are generally but not universally

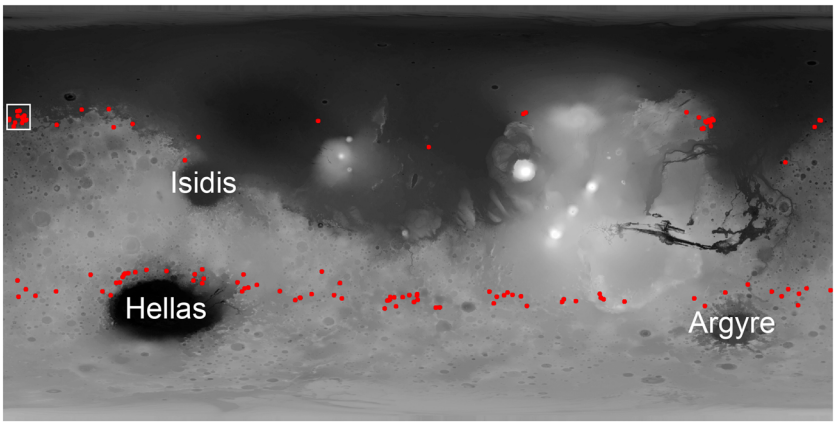

Figure 3. Global survey of CTX data shows clusters of FSVs (red dots) that occur in a tight latitude band between ~35–42° in the northern and southern hemispheres. Northern Arabia Terra, roughly 30–40°N between 0 and 10°E, has one of the highest concentrations of FSVs on Mars (white box, see Figure 4). Mars Global Surveyor MOLA Elevation Model (90°N to −90°N, −180°E to 180°E).

associated with high-relief surfaces, such as the interior and exterior slopes of impact craters. Some terminate in fans or deltas as seen in Xanthe Terra [*Hauber et al*., 2013], the sparse network feeding the Eberswalde crater delta [*Howard et al*., 2005], connecting fans to the interior rim of Bakhuysen crater [*Moore and Howard*, 2005] and on the rim and exterior of the Late Noachian to Hesperian-age Gale crater [e.g., *Grant et al*., 2014; *Palucis et al*., 2014] (Figure 1).

2.2. Occurrence and Global Distribution of FSVs

FSVs occur in a variety of settings including the flanks of volcanoes [*Fassett and Head*, 2006, 2007; *Gulick and Baker*, 1990; *Gulick*, 2001a], crater interiors [*Dickson et al*., 2009; *Hobley et al*., 2014; *Howard and Moore*, 2011; *Parsons et al*., 2013], intercrater plains, and on the ejecta of young impact craters [*Jones et al*., 2011; *Mangold*, 2012; *Mangold et al*., 2012; *Morgan and Head*, 2009]. These valleys are also commonly associated with Amazonian-age glacial features such as lobate debris aprons, concentric crater fills, viscous flow features, and lineated valley fills [*Adeli et al*., 2016; *Fassett et al*., 2010], and in some cases the valleys may represent a period of reactivation of the Noachian-Hesperian aged valley networks that locally terminate as small deltas in Hesperian basins [*Irwin et al*., 2005a].

FSVs are modified at the submeter to meter scale by "pasted on" deposits and hummocky topography related to "terrain softening," a nonfluvial process that modified Noachian to early Hesperian craters and may have continued into the late Amazonian in middle- to high-latitude locations [*Berman et al*., 2009; *Mustard et al*., 2001; *Soderblom et al*., 1973; *Willmes et al*., 2011] (Figure 1d). This latitude-dependent mantle may have formed as a result of obliquity variations that mobilized water ice from the poles to the midlatitude regions [e.g., *Head et al*., 2003; *Laskar et al*., 2004]. In most cases, much of the modification related to the latitude-dependent mantle occurred prior to the formation of FSVs based on their superposition into the softened terrain and their largely fresh appearance at the resolution of CTX images (Figure 1d).

A global survey of CTX images as of late 2012 that builds upon previous mapping [*Fassett et al*., 2010; *Mangold*, 2012] reveals that FSVs are widely distributed (Figure 3). The valleys occur in a latitude band between ~35 and 42° in the northern and southern hemispheres and are most easily recognized where they incise into the smooth latitude-dependent mantle (which occurs poleward of ~35° in both hemispheres). Valleys in the northern hemisphere generally occur along the dichotomy boundary with clusters in Tempe Terra and northern Arabia Terra (Figure 3). FSVs commonly occur in clusters that range from several valleys on the ejecta of a single impact crater to widely distributed valleys. FSVs also occur in the equatorial regions (e.g., Gale crater and surroundings; Figure 1c) but are often hard to distinguish from Noachian valley networks.

2.3. The Northern Arabia Terra Landscape and Associated Landforms

Northern Arabia Terra in U.S. Geological Survey quadrangle Ismenius Lacus (Mars Chart 05) records a long history of aqueous activity from the Noachian through the Amazonian [*Mangold and Howard*, 2013].

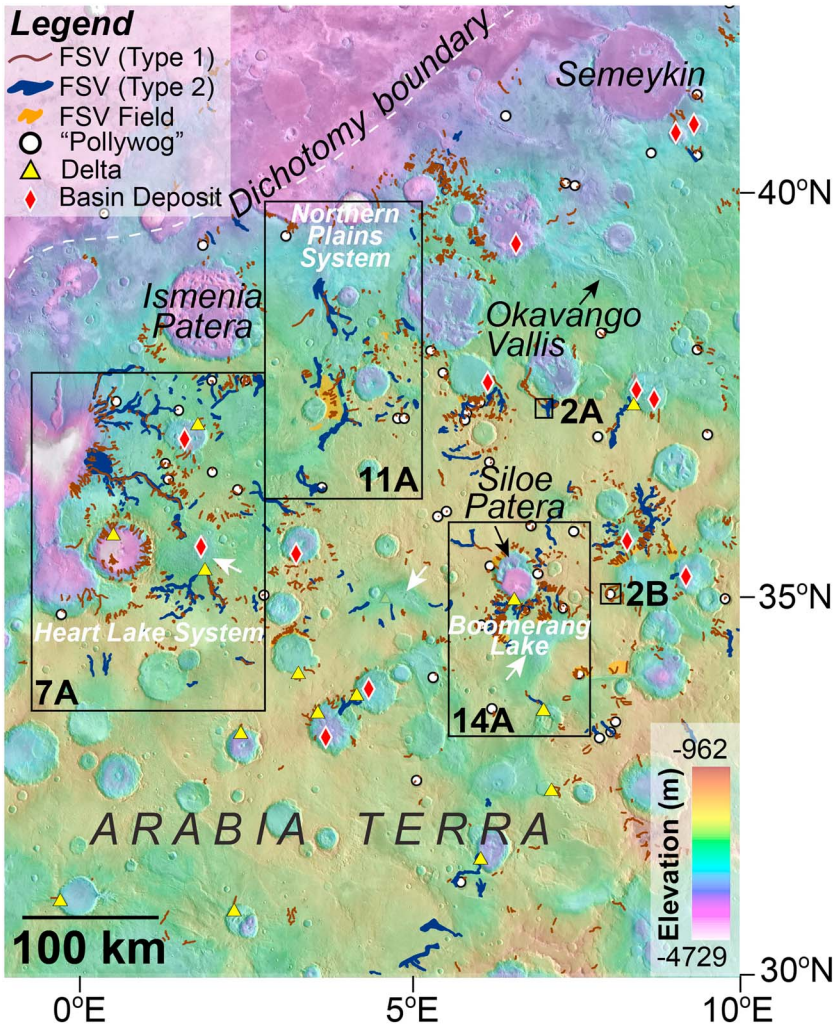

Figure 4. Study region in northern Arabia Terra in southwest Ismenius Lacus (see Figure 3 for context) with major place names labeled for reference. South of the dichotomy boundary; this softened cratered landscape has many broad, Noachian-aged depressions (e.g., white arrows) and is dissected by FSVs (brown and blue lines are Types 1 and 2, respectively; see Figure 2a). Some FSVs breach crater rims and terminate in small deltaic deposits (yellow triangles; see Figure 2c) whereas other FSVs occur as single channels that extend outward from craters rim (pollywogs) implying overflow of a crater lake (white circles; see Figure 2b). A FSV "field" indicates areas that are heavy dissected. Basin floor deposits are indicated by red diamonds (Figures 2c, 2d and 8b). Black boxes show locations of Figures 2a, 2b, 7a (Heart Lake valley system), 11a (Northern Plains valley system), and 14a (Boomerang Lake valley system). MOLA topography over subframe of Thermal Emission Imaging System (THEMIS) Day IR mosaic. The width of Type 1 FSVs is exaggerated for clarity in regional maps (Figures 4, 6, 7, 11, and 14).

Located south of the dichotomy boundary, the study region (~30–40°N between 2°W and 10°E) is characterized by a low-lying (< -2 km relative to the MOLA datum) cratered landscape that contains putative ancient volcanic calderas mapped as Ismenia and Siloe Patera [*Michalski and Bleacher*, 2013] (Figure 4). Several large depressions ~30 km wide and up to 1 km deep formed by deeply seated subsidence in the Noachian prior to the formation of the FSVs [*Mangold and Howard*, 2013]. Well-developed Noachian valley networks are notably absent from this terrain [e.g., *Luo and Stepinski*, 2009; *Hynek et al.*, 2010], but the late Noachian-early Hesperian Okavango Vallis outflow system is located on the eastern margin of the study area [*Mangold and Howard*, 2013] (Figure 4).

This area contains a high concentration of FSVs, some of which incise crater rims. Craters with an outlet valley, characterized by a single valley extending outward from the rim and no inflowing valleys are informally named "pollywogs" (Figure 2b). Pollywog craters most commonly have 1 valley but some craters have 2–3 valleys extending outward from their rims, with the channel generally oriented toward the nearest topographic low.

Lobe or fan-shaped deposits within craters at the mouth of inlet valleys are inferred to be sedimentary (Figures 2c, 4 and 6) [e.g., *Goudge et al*., 2015]. These landforms are consistent with a fluvial fan or deltaic origin based on their morphologic form (some of which have steep depositional fronts [e.g., *Di Achille and Hynek*, 2010]), hints of layering, and their position well above the crater floor that likely records deposition into standing bodies of water.

Landforms identified and mapped as "basin floor deposits" occur on the lowest floor elevation of some craters and depressions in the study region (Figures 2c, 4, and 6). These deposits not only tend to be concentric to the edges of their respective host basin but also occur as isolated deposits. The margins and (or) surface of the basin floor deposits have subparallel to parallel fractures. A scarp along the basin floor deposit adjacent to the deepest (> -3160 m) depression on the floor of basin C is characterized by fine-grained, massive, and repetitive packages of ~10 m thick medium-toned layers separated by thinner darker-toned layers (Figure 2d). The fine-grained, horizontal, layered nature of these deposits and their association with basin interiors is consistent with a lacustrine origin. The relative age and the relationship of these basin floor deposits with the timing of FSV activity is uncertain.

3. Data and Methods

3.1. Geomorphic Mapping

FSVs in northern Arabia Terra were mapped in ArcGIS utilizing processed and projected images from CTX and High Resolution Imaging Science Experiment (HiRISE, ~0.25 m pixel scale) [*McEwen et al*., 2007] on the Mars Reconnaissance Orbiter, images from the High Resolution Stereo Camera (HRSC, ~10 m pixel scale) [*Neukum et al*., 2004] on Mars Express, and topographic data from the Mars Orbiter Laser Altimeter (MOLA) on Mars Global Surveyor [*Smith et al*., 1999]. CTX and HiRISE digital terrain models (DTMs) were not available in the region at the time of publication, and the one HRSC DTM did not offer higher-resolution data. We investigated a broader region, but the final extent of the study area selected for detailed mapping, ~30–40°N between ~0 and 10°E, was determined by the decreasing occurrence of FSVs and associated landforms outside of these bounds.

3.2. The Hydrological Routing Model

To constrain the hydrologic regime associated with the formation of FSVs in our study area, we utilized the hydrologic routing model after *Matsubara et al*. [2011, 2013] to (1) estimate the flow of surface water across the landscape and (2) quantify the area and volume of any model-predicted water-filled depressions that have associated geomorphic evidence of valley incision. The model utilizes MOLA topography to route water and assumes a steady state balance between evaporation and runoff over multiyear time periods. The model also assumes spatially uniform precipitation, runoff, and evaporation from standing water. Due to uncertainties associated with the absolute magnitudes of precipitation, runoff, and evaporation, these variables are replaced by the "*X* ratio," which serves as a proxy for climatic conditions [*Matsubara et al*., 2011, 2013]. The *X* ratio is defined as:

$$X = \frac{(E - P)}{RP}$$

where E = evaporation from lakes, P = precipitation, and R = fraction of precipitation resulting in runoff from nonsubmerged locations. Small *X* ratio values (e.g., $X = -1$) correspond to an environment with total runoff and no evaporation. As the *X* ratio increases, the corresponding climate becomes more arid, fewer basins overflow, and drainage networks become more fragmented. As explained in *Matsubara et al*. [2013], the value of the *X* ratio does not correspond to any one combination of precipitation, runoff, and evaporation, such that several combinations of values for these variables could result in the same *X* ratio. For example, an *X* ratio of ~2.2 could result from $P = 0.5\ \mathrm{m\ yr^{-1}}$, $R = 0.45$, and $E = 1\ \mathrm{m\ yr^{-1}}$, or $P = 1.45\ \mathrm{m\ yr^{-1}}$, $R = 0.17$, and $E = 2\ \mathrm{m\ yr^{-1}}$ [after *Matsubara et al*., 2013]. Several simulations were run using a range of *X* ratio values from -1 (runoff-dominated) to 6 (evaporation-dominated with little runoff) to constrain how wet the environment had to be to match the location and morphology of FSVs preserved in the landscape, including overflow of inferred lakes embedded in long FSV systems.

For the deltas in our study area, the elevation of each upper delta platform (hereafter referred to as "platform") corresponding to the predicted water level at the time of active fan deposition was extracted from MOLA data

overlaid on projected CTX images in *JMars* (an online geospatial information system developed by Arizona State University [*Christensen et al.*, 2009] (Table 2). The platform elevation represents the maximum water level associated with delta formation [e.g., *Di Achille and Hynek*, 2010]. In the cases where MOLA altimetry tracks intersected the delta platform, individual MOLA shot points were used to extract elevation data. In all other cases, gridded MOLA data were used to estimate the platform elevation. For 12 of the basins hosting deltas, the hydrologic model was queried to determine the *X* ratio value that corresponds to the maximum lake level estimated from the elevation of the delta platform.

3.3. Crater Statistics and Relative Ages

The timing of fluvial activity was constrained by estimating the age of 22 craters (diameter range ~4–48 km) in the study region whose ejecta preserve a range of fluvial modification. We only considered craters with well-preserved ejecta, and we determined the crater size-frequency distributions of smaller craters superimposed on the ejecta itself. The onset of fluvial activity is bound by the range in age of ejecta deposits incised by FSVs (based on the observation that valleys incise into the ejecta and are therefore younger), and the end of fluvial activity is derived from the age of the ejecta deposits that are fluvially unmodified. Uncertainties in individual derived ages due to relatively small counting areas associated with the crater ejecta deposits suggest that FSV incision may have begun and ended somewhat earlier and later, respectively, but the collection of data provides meaningful insight into the timing of fluvial activity that formed the FSVs and associated landforms.

The craters superimposed on the continuous ejecta blankets were counted on projected CTX images (released as of July, 2014) using CraterTools software [*Kneissl et al.*, 2011] in Environmental Systems Research Institute's ArcGIS. Craterstats software was used to compile reverse cumulative histograms using pseudo log bins to interpret relative absolute ages [*Michael and Neukum*, 2010] based on the chronology function of *Hartmann and Neukum* [2001] and production function from *Ivanov* [2001]. Relative ages were verified using incremental plots based on the variable bin-size method of *Hartmann* [2005] (see supporting information). The maximum modeled absolute ages were estimated from the largest craters that provided the best fit for the expected production population. The linear density of Type 1 FSVs for each ejecta was determined by dividing the cumulative length of Type 1 FSVs incised into the ejecta by the area of the ejecta (Table 3). Each crater ejecta was classified as having a high linear density of FSVs (class 1, $>0.04\,km^{-1}$), a low linear density of FSVs (class 2, $<\sim0.03\,km^{-1}$) or no FSVs (class 3).

4. Observations and Inferences

4.1. Distribution and Nature of FSVs and Associated Deposits in Northern Arabia Terra

Mapping indicates FSVs in the study area are widespread and characteristically start abruptly on uplands and steeper slopes and terminate near the margins of numerous depressions in the landscape (Figure 4). Most FSVs are relatively short and terminate on the flanks of local basins above the basin floor. Some FSV segments, however, are inferred to bridge depressions in the landscape to form long (>150 km) valley systems (including the informally named "Heart Lake" and "Northern Plains" described in sections 4.3 and 4.4, respectively). In such locations the intervening depression floors are undissected. These longer and more complex valley systems tend to have Type 1 valleys incised into Type 2 valleys (Figure 4) and often have tributaries. The informally named "Boomerang Lake" system is not a long, integrated system but provides additional evidence for valley incision related to basin overflow (section 4.5).

Several crater rims are incised by FSVs. Fifty-nine "pollywog" craters (Figure 2b) identified in the study region have an average diameter of 3.9 km (diameter range 0.6–13.4 km), and the majority (61%) of pollywogs occur between 35°N and 40°N (Figure 4). Approximately 31 craters have inlet valleys, of which 10 terminate in sedimentary deposits inferred to be deltaic in origin (Figures 2c and 4). Three additional craters host deltas that originate from valleys along the interior rim of the host crater (i.e., the host crater rim is not breached). Craters hosting deltas have an average diameter of ~29 km (diameter range is 11–48 km) and occur between 31°N and 37°N (average 34°N). Similar landforms associated with the older Okavango Vallis outflow system [*Mangold and Howard*, 2013] were not considered. The deltas are generally small (average < 3 km in length and < 2.5 km in width, Table 2). All of the deltas are located between ~200 and 850 m above the floor of their respective host craters (Table 2).

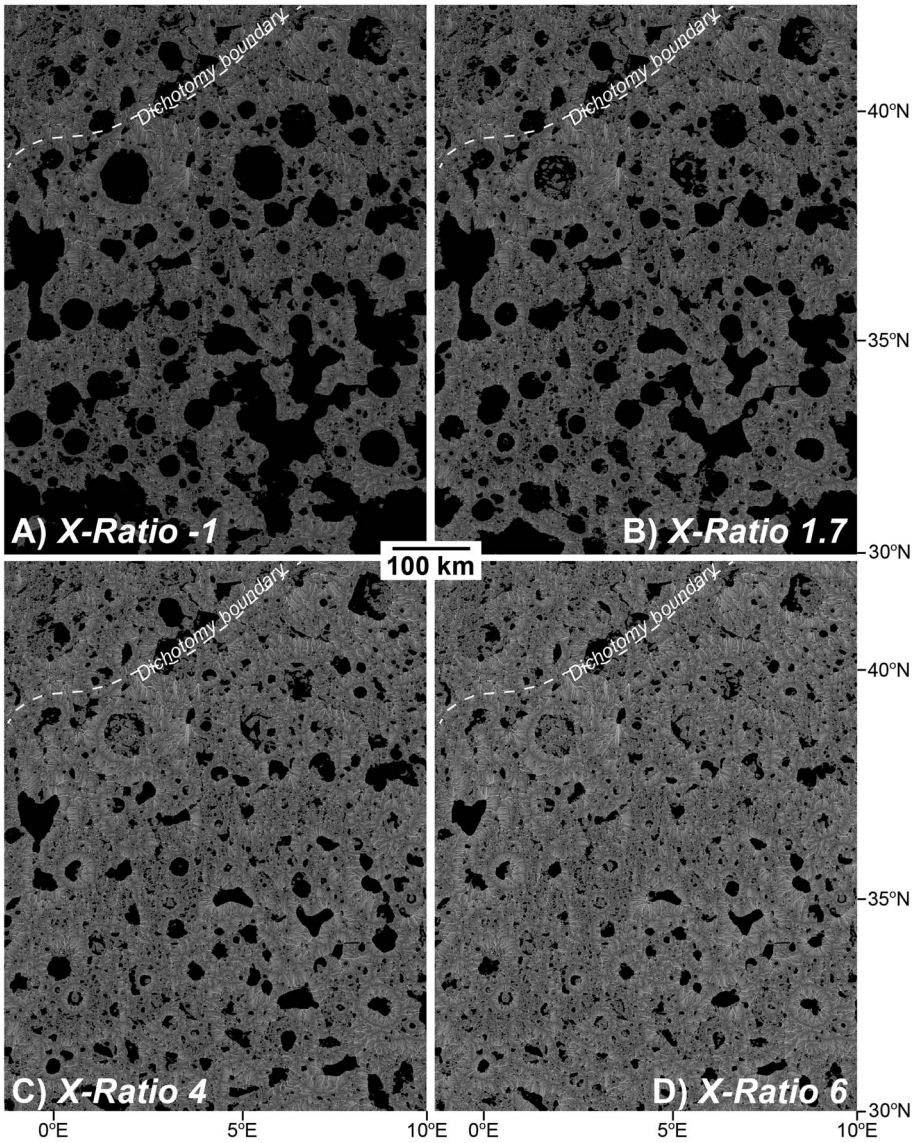

Figure 5. The regional surface hydrology model results for the study area (see Figure 4 for context) for *X* ratio [*Matsubara et al.*, 2011, 2013] values equal to (a) −1, (b) 1.7, (c) 4, and (d) 6. Results of *X* ratio ~2.2 shown in Figure 6. White-gray lines are predicted annual surface flow with brightness proportional to the logarithm of discharge under spatially uniform annual precipitation, runoff, and evaporation. As evaporation becomes more important relative to other parameters, the environment becomes more arid and fewer basins will overflow, and drainage networks become more fragmented [*Matsubara et al.*, 2011]. Predicted submerged locations are black.

4.2. Hydrological Model

The output of the regional surface hydrology model, based on runoff versus evaporation (*X* ratio) [*Matsubara et al.*, 2011, 2013], shows inferred flow paths across the landscape and several submerged basins (Figure 5). As the *X* ratio increases, the predicted submerged regions decrease in volume and areal extent. At an *X* ratio of ~2.2, the model-predicted location and extent of the submerged basins corresponds remarkably well to most downstream terminations of FSVs (Figure 6).

All of the deltas occur along the interior walls of model-predicted submerged basins (Figure 6). The *X* ratio representing the modeled lake level corresponding to the platform elevation of 12 deltas in the study region have average value of 2.5 (Table 2). This result is consistent with the *X* ratio value of ~2.2 to 4 that corresponds to overflow of filled basins in the region (Table 1 and Figure 6).

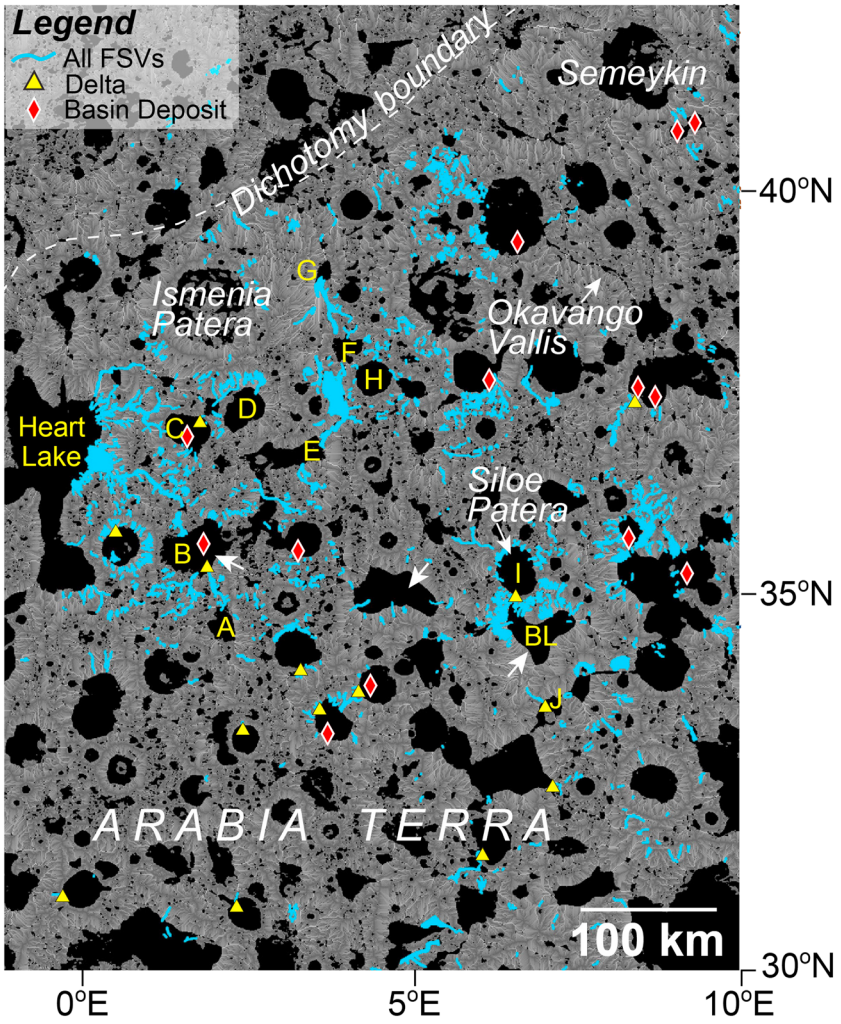

Figure 6. All FSVs mapped on the basis of morphology (blue lines, see Figure 4 for context) on top of the regional hydrologic routing model where the *X* ratio is ~2.2 (see Figure 5 for flow path and lake explanation). Most FSVs terminate at the margins of the model-predicted submerged basins, and some valley segments connect to form longer systems consistent with connection by overflow across interspersed lakes. The width of FSVs is exaggerated for recognition quality. White arrows indicate the same broad depressions labeled in Figure 4 that would be submerged. Deltas (yellow triangles) and basin floor deposits (red diamonds) occur along lake margins and floors of submerged basins, respectively. Submerged basins discussed in the text are labeled as A–J, Boomerang Lake (BL), and Heart Lake (see Table 1).

4.3. Heart Lake Valley System

The informally named Heart Lake valley system is ~150 km long and consists of two main FSV segments (Figure 7). This system originates from a topographic depression (basin A) near 34.8°N, 2.1°E and incises northward for ~38 km before emptying into basin B. The valley is interpreted to reappear ~30 km to the northwest and flows west-northwest for ~100 km (average gradient ~0.005), terminating near 36.7°N, 359.9°E in a heart-shaped depression referred to as Heart Lake (Figure 7).

The FSVs at the headwaters of this system originate at the northern margin of the model-predicted submerged basin A, but the extent of drainage entering this basin from the south is obscured by a subsequent impact crater (Figure 7). The hydrologic routing model predicts a volume of ~12 km^3 for basin A, which would overflow at *X* ratio values ≤ 4 (Table 1). The ~1 km wide valley emerging from the northern margin of basin A has a ~100 m wide interior valley and terminates near the southern boundary of the model-predicted margin of basin B, forming a low-relief fan-shaped deposit (Figure 8).

Basin B is an irregularly shaped depression with a maximum depth of ~400 m. The southern margin of basin B received flow from basin A as well as other contributing valleys (Figure 7a). The basin has been slightly

Table 1. Characteristics of Model-Predicted Paleolakes in the Heart Lake, Northern Plains, and Boomerang Lake Valley Systems Based on Hydrologic Modeling Results

Basin	Maximum Lake Surface Elevation (m)	Maximum Lake Volume (km^3)	Maximum Lake Area (km^2)	Average Lake Depth (m) (vol/area)	Maximum Lake Depth (m)	*X* Ratio at Lake Overflow
			Heart Lake Valley System (Figure 7)			
Basin A	−2369	12	366	30	310	≤4
Basin B	−2505	188	1409	130	401	≤2.25
Basin C	−2673	217	735	30	571	≤2.75
Basin D	−2663	29	654	40	166	≤4
Heart Lake	−3342	2790	7038	400	982	≤2.25
			Northern Plains Valley System (Figure 11)			
Basin E	−2528	1280	8643	150	783	≤2.5
Basin F	−2733	57	1195	50	139	≤4
Basin G	−3051	13	648	20	68	−1
Basin H	−2616	937	2152	440	842	≤2.75
			Boomerang Lake Valley System (Figure 14)			
Boomerang Lake (intact rim before overflow)	−2385	424	2334	182	571	≤1.25
Boomerang Lake (after overflow)	−2385	101	905	112	360	≤1.25
Basin I (intact rim before overflow)	−2385	1340	3563	376	1547	No overflow
Basin I (after overflow)	−2385	1350	3582	377	1547	No overflow

modified by the ejecta from the 48 km diameter crater to the west and rounded deposits occur along the lowest elevations of the basin floor (Figure 7b). These isolated deposits are a few kilometers in width and up to ~70 m in height. The relationship between these deposits and FSV formation is unclear; it is possible that these deposits are remnants related to the final waning stages of the lake that occupied this basin. These landforms are mapped as basin floor deposits, and similar deposits occur in other model-predicted, water-filled basins in the study area (Figures 2c, 2d, 4, and 6).

The steady state hydrologic model predicts overflow along the northern margin of basin B at a volume of 188 km^3 for all *X* ratio values ≤ 2.25 (Table 1). The extent and elevation of this lake corresponds to morphologic evidence of overflow along the northern margin of basin B (Figure 9). The mouth of the outlet valley is ~4 km wide, and the channel appears deeply incised. Roughly ~10 km from the overflow breach a meander exhibits streamlined depositional bars within the valley (Figure 9b). Locations along the valley where sidewalls are less defined, incised channels are absent, and possible fan-like depositional forms occur corresponds to model-predicted ponded water along the flow path (*X* ratio ~2.2; Figure 9a). The valley emerging from the southern margin of basin B continues ~100 km to the west-northwest and incises into the eastern margin of Heart Lake (Figure 7).

The steady state hydrologic model predicts overflow along the northern margin of Heart Lake at a volume of 2790 km^3 for all *X* ratio values ≤ 2.25 (Table 1). The predicted lake level in Heart Lake at an *X* ratio of ~2.2 is −3342 m (dashed line in Figure 7d), which corresponds well to the elevation of the broad, upper incised surface near the margin of Heart Lake. Near an elevation of −3350 m, a knick point in the profile likely corresponds to a change in base level in Heart Lake. The valley downcuts ~200 m to an elevation near −3547 m along the floor of Heart Lake, which corresponds to an *X* ratio of ~2.7 that has a corresponding model-predicted lake surface of −3513 m. Between *X* ratios of ~2.25 and ~2.7, the model predicts the volume and lake surface in Heart Lake would decrease by ~1110 km^3 and ~172 m, respectively, consistent with the amount of valley downcutting along the eastern margin of Heart Lake (Figure 7d). The roughly circular deposit on the floor of Heart Lake at the valley terminus appears deflated and deformed with cracks and upturned margins, perhaps indicative of sediment-ice interaction (Figure 7d). A channel along the western margin of this enigmatic deposit is associated with rounded low-relief deposits that extend ~8 km onto the floor of Heart Lake (Figure 7d). We interpret these landforms to be analogous to step deltas deposited during fluctuations in lake levels.

Several FSVs are incised between Heart Lake and basin C, located ~60 km to the east of the Heart Lake delta (Figure 7). The model predicts basin C at its largest extent would hold ~217 km^3 of water, overflowing for *X*

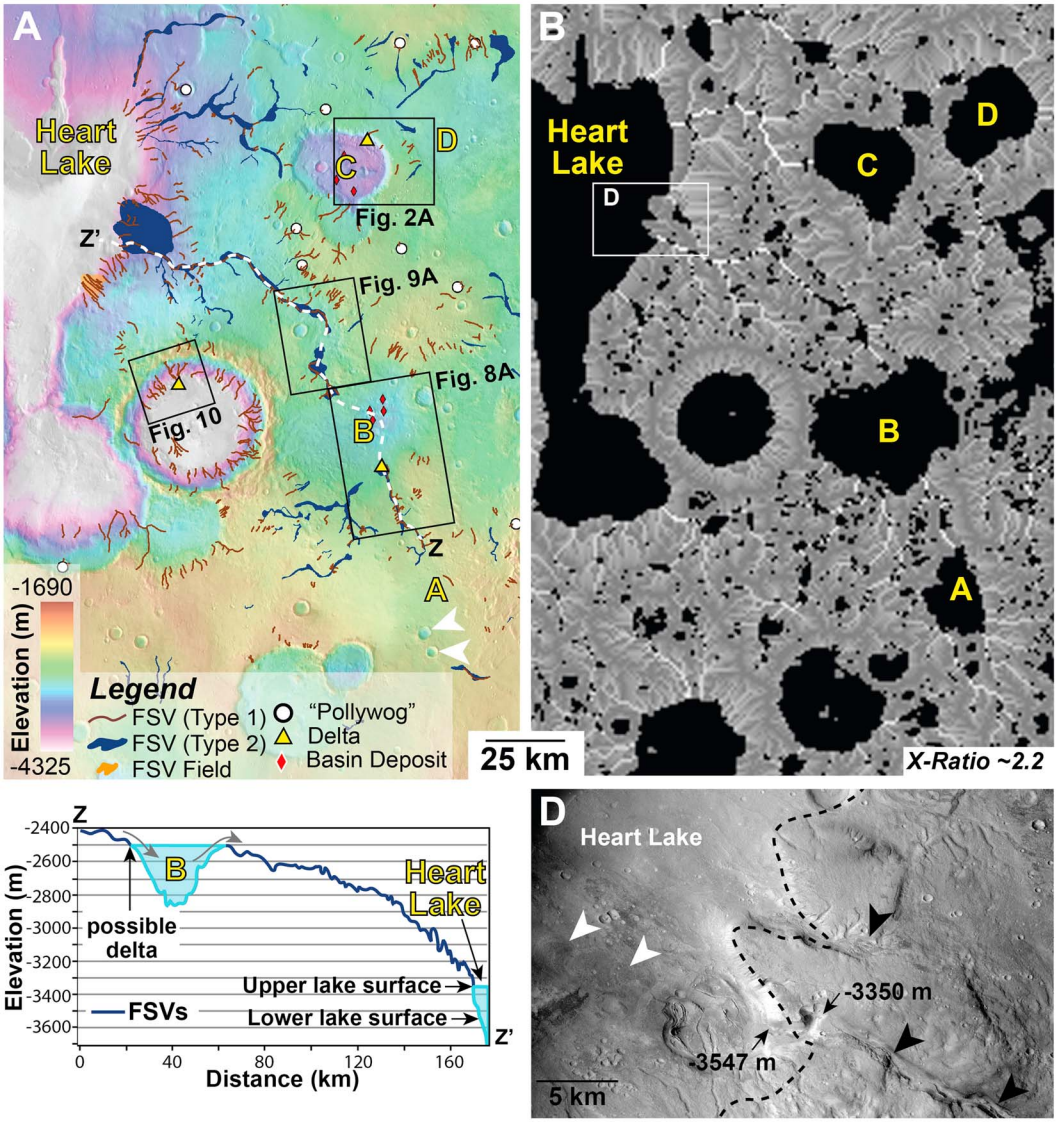

Figure 7. (a) Regional view (see Figure 4 for context) of the informally named Heart Lake valley system where two main FSV segments connect to make a 150+ km long valley system (white dashed line). FSVs commonly disappear and reappear across depressions in the landscape (e.g., basin B) that were likely filled with (ice-covered?) lakes at the time of valley formation. Arrows indicate younger craters that obscure the amount of drainage entering basin A. Black boxes show locations of Figures 2a, 8a, 9a, and 10. MOLA over THEMIS Day IR, centered near 35.91°N, 1°E. North to top. (b) Regional hydrologic modeling predicts location, size, and volume of filled depressions and flow paths across the landscape in the area of Figure 7a (see Figure 5 for flow path and lake explanation and Table 1). Model result equivalent to an *X* ratio value of ~2.2 (see text), the point at which basin B would have overflowed along its northern margin and transported sediment into Heart Lake. Submerged basins A, C, and D likely contributed to the Heart Lake valley system although morphologic evidence of overflow from basin C is not convincing. The predicted extent and overflow of basin B is consistent with the preserved morphology (see Figure 9). Box shows location of Figure 7d. Centered near 35.91°N, 1°E, north to top. (c) Profile of transect *Z* to *Z'* in Figure 7a indicating regional gradient toward Heart Lake. Valleys flowed into and out of basin B and terminate in Heart Lake. (d) Valleys (black arrows) at the terminus of the Heart Lake valley system downcut ~200 m to the floor of Heart Lake, consistent with a change in base level. Rounded lobes (white arrows) on the floor of Heart Lake. Predicted lake level at an *X* ratio of ~2.2 (dashed line) corresponds well to the depth of valley incision. Subframe of CTX 17_007519_2147, 5.96 m scaled pixel scale. North to top.

ratio values of ≤ 2.75 (Table 1). Evidence indicative of overflow along the western margin of basin C is not convincing due to the lack of a deeply incised channel as well as the absence of a fan at the valley terminus (Figure 7). Morphologic evidence of water flowing from basin D to basin C (via a small depression in between basins C and D) is supported by the valley and associated delta on the northeastern rim of basin C (Figure 2c).

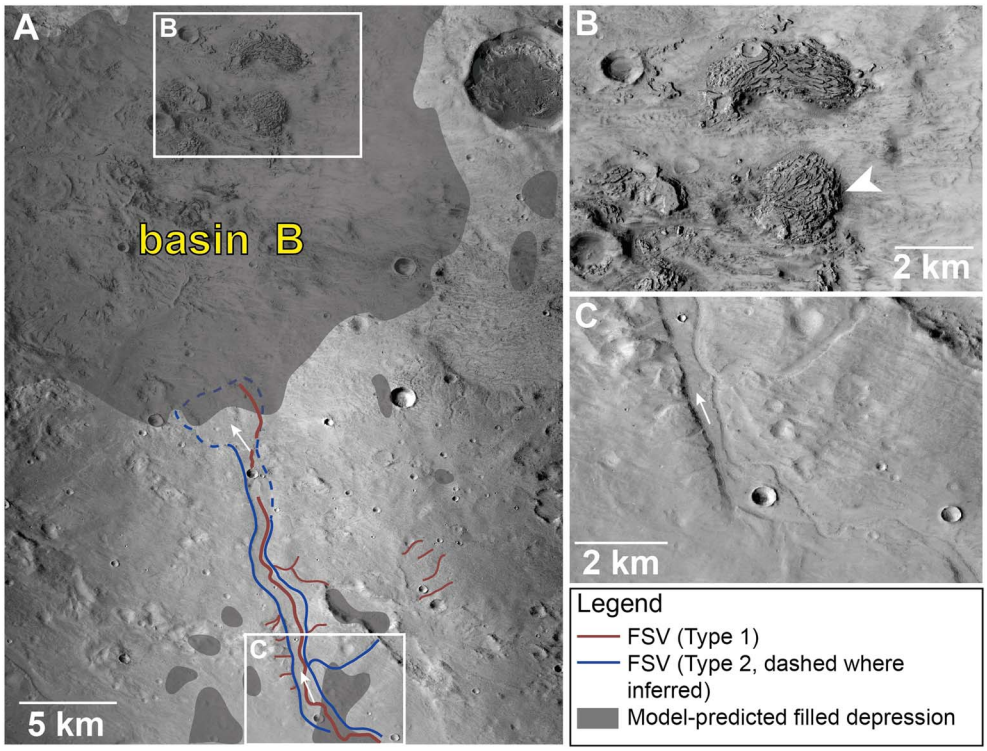

Figure 8. (a) Geomorphic map of the southern inlet into basin B from basin A within the Heart Lake valley system (see Figure 7a for context). The FSV disappears along the predicted margin of the submerged basin (shaded) at an *X* ratio of ~2.2 (see Figure 7b for context). Arrows indicate flow direction, and boxes show location of Figures 8b and 8c. Subframe of CTX P17_007809_2169 (5.89 m scaled pixel width). (b) Dark-toned, possibly ice-rich layered sediment occurs along the deepest floor of basin B, near an elevation of −2850 m relative to the MOLA datum. The rounded deposit (white arrow) is a few kilometers wide and rises about ~70 m from the basin floor. These deposits could be related to final stages of the lake that occupied this basin, or possibly remnants of a larger deposit. Similar deposits occur in basin C (Figures 2c and 2d) and elsewhere in the region (Figures 4 and 6) along the floors of model-predicted submerged basins. (c) Detail of ~17 km long valley leading to southern margin of basin B; arrow indicates northward direction of flow. North to top in all images.

The *X* ratio associated with a modeled lake surface of −3048 m (based on the elevation of the lobe surface) is ~3.5, implying the basin hosted a lake roughly 270 m deep. Basin D was small, with a model-predicted maximum volume and depth of 29 km^3 and 166 m, respectively, overflowing at *X* ratio values ≤ 4 (Table 1).

One of the younger, large (48 km diameter) craters in the study area is located between Heart Lake and basin B (35.6°N, 0.55°E; Figure 7). The fresh-looking ejecta from this Amazonian- to Hesperian-aged [*Tanaka et al.*, 2014] crater is dissected by the Heart Lake valley system (Figure 7). The interior rim of this crater is dissected by FSVs that terminate in several fan-shaped deposits, including a steep-front step delta on the crater's northwestern rim (Figure 10). This delta extends ~3.5 km from the apex (elevation of ~ −3683 m) to distal margin (elevation of −3930 m) with an overall gradient of ~0.07. The delta was fed by numerous incised valleys on the interior crater rim, but distributary channels on the fan surface are not apparent. The fan surface at HiRISE scale has numerous small craters and is not heavily modified by midlatitude mantling material. There are at least five steps on the delta front that decrease in elevation from the apex to the toe of the deposit, with elevations decreasing between ~20 and 80 m per step (average ~50 m, based on MOLA shot points). The steady state hydrologic model predicts this 48 km diameter crater would not host an overflowing lake unless the *X* ratio dropped to the unrealistic value of −1 (Figure 7b), consistent with the absence of a breach in the crater rim. The *X* ratio corresponding to the model predicted lake surface associated with the platform elevation of the step delta is ~1.7, implying the crater hosted a ~575 m deep lake (Table 2).

Several light-toned, sinuous ridges appear to emerge from the distal end of the delta and intersect a ~10 km long east-west oriented sinuous ridge with a gradient of 0.02 (Figure 10). The sinuous ridges at the delta front

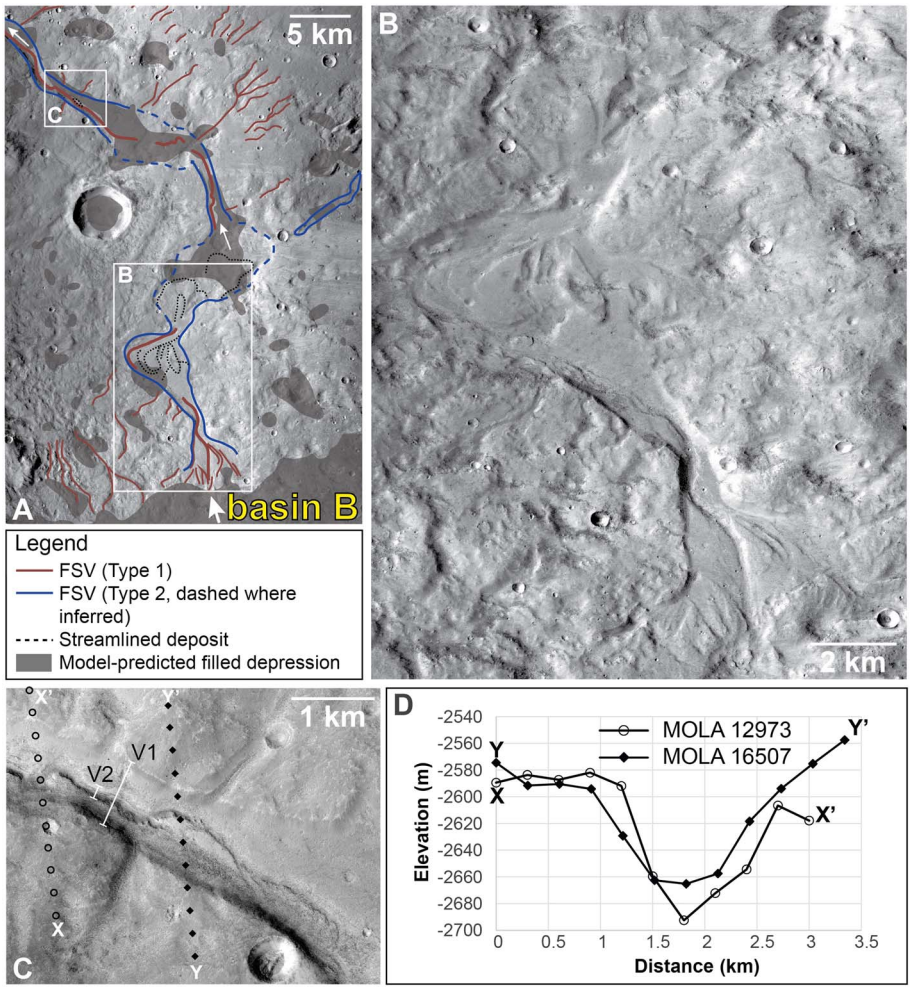

Figure 9. (a) Geomorphic map of the outlet valley on the northern margin of basin B within the Heart Lake valley system (see Figure 7a for context) detailing the FSVs and associated streamlined features (black dotted lines). The valley coincides with the model-predicted lake margin (shaded) at an *X* ratio of ~2.2 (see Figure 7b for context). Arrows indicate flow direction and boxes show location of Figures 9b and 9c. Subframe of CTX B18_016815_2151 (5.8 m scaled pixel width). (b) The FSV on the downstream side of basin B meanders and exhibits streamlined forms, scours, and streamlined depositional channel bars. Subframe of CTX B18_016815_2151 (5.8 m scaled pixel width). (c) Representative widths of the main valley (V1) and interior valley (V2) used to estimate discharge rates (section 5). Transect *Y* to *Y*′ and *X* to *X*′ from MOLA transects 16,507 and 12,973, respectively (see profiles in Figure 9d). Subframe of HiRISE ESP_033245_2165 (59.7 cm scaled pixel width). (d) Estimated from MOLA data, the main channel is roughly 1000 m wide and 70 m deep, and the incised channel is ~90 m wide (assumed to be half of the channel wall-to-wall width) and ~2–8 m deep. North to top in all images.

and the ridge on the crater floor begin near a common elevation between −3890 and ~ −4000 m, correlating to the margin of the lowest part of the crater interior that occupies the westernside of the crater floor. The origin of the sinuous ridges and their relationship to the delta on the northwestern rim remains unclear. The ridges could be inverted fluvial channels, but if so, they would have to consist of much coarser grains relative to the adjacent delta so that the channels could erode and become inverted without significant observed modification of the delta. Alternatively, the channels could be related to flow beneath a now-absent ice cover, analogous to eskers [e.g., *Hobley et al.*, 2014]. Lastly, narrow channels could have eroded into the surface of an ice-covered lake, and subsequent "let down" of the channel during melting or sublimation of the ice could form landforms analogous to kames. This explanation has some deficiencies because kame deposits are generally irregular due to the unevenness of ice melting, and if the ice-covered lake were level, a fan or delta may be expected to form along the margin of the ice where the sediment-laden flows debouched.

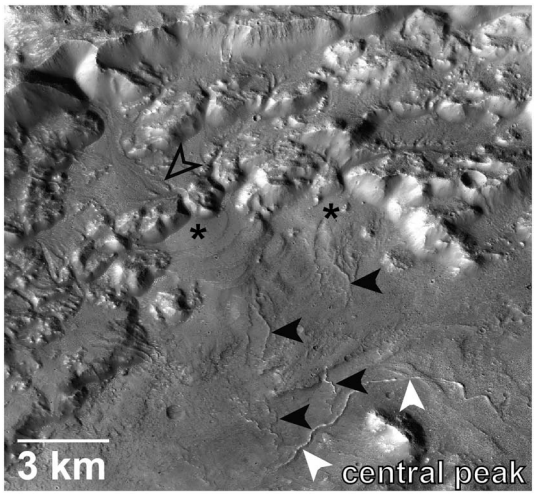

Figure 10. The ~48 km diameter crater near 35.6°N, 0.55°E preserves myriad fluvial landforms (see Figure 7 for context) including FSVs (e.g., hollow black arrow) and deltas (asterisk sign). Located between Heart Lake and basin B, the hydrologic model predicts this crater would have been submerged but did not overflow (Figure 7b). The step delta on the northern rim supports evidence for fluctuating water levels within the crater. Sinuous ridges (white and black arrows) flow downhill into a local topographic depression along the western crater floor. Ridges appear to emerge from the base of the deltas (black arrows) and join the main ridge (white arrows) near the central peak of the crater. Subframe of CTX image D04_028841_2159 (5.86 m scaled pixel width). North to top.

4.4. Northern Plains Valley System

The informally named Northern Plains valley system is approximately 120 km northwest of basin B and originates near 36.9°N, 3.56°E (Figure 11). This northward flowing, ~200 km long system consists of three main FSV segments separated by depressions in the landscape, ultimately terminating at the dichotomy boundary near 39.9°N, 3.6°E (Figure 11).

The southernmost FSV segment in this system originates from the northeastern margin of basin E, which has a model-predicted volume of 1280 km^3 and would overflow for X ratio values ≤ 2.5 (consistent to the X ratio associated with the predicted overflow of basin B in the Heart Lake system, Table 1). The ~1 km wide outlet from basin E incises northward with an average gradient of 0.003 for roughly 70 km before disappearing at the margin of a ~25 km wide depression, basin F (Figure 11). The valley segment between basins E and F is predominantly a wider Type 2 valley that becomes incised with an interior valley just before debouching into the southern margin basin F (Figure 12). Light-toned, possibly layered deposits occur along the northern margin of basin F where the basin is deepest (Figure 13). The model-predicted volume and X ratio where overflow would occur in basin F is 57 km^3 and ≤ 4, respectively (Table 1). A crater hosting basin H to the southwest of basin F (Figure 11) may have stored a significant amount of water (~937 km^3) that would have overflowed at X ratio values of ≤ 2.75 (Table 1). The northwestern, lowest portion of the rim of basin H is dissected by several FSVs, but the sense of flow into or out of basin H is unclear. No delta occurs in the crater interior where the FSVs erode the basin margin. One FSV on the northwestern crater rim, however, is associated with smooth, light-toned material near the model predicated shoreline of basin F (see CTX D19_034669_2178) that might be a sedimentary deposit related to overflow of basin H.

Table 2. Estimation of X Ratios and Associated Lake Depths Based on the Elevation of the Delta Platform

Delta Location	Delta Length (km)	Delta Width (km)	Elevation of Delta Platform (m)	X ratio From Platform Elevation	Predicted Lake Depth (m)
31.3°N, 59.9°E	2.3	1.5	−2668[a]	1.90	444
31.2°N, 2.4°E	4.7	3.5	−2704[a]	3.25	222
31.8°N, 5.98°E	4	3	−2895[b]	2.75	645
32.7°N, 7.02°E	2	2.58	−2489[a]	2.12	264
33.7°N, 6.9°E (basin J; Figure 14e)	2	1.3	−2446[b]	1.38	368
35.0°N, 6.5°E (basin I; Figure 14c)	2	2.8	−3075[a]	3.92	857
33.4°N, 2.4°E	2.5	3.5	−2890[a]	2.26	644
33.6°N, 3.6°E	1.7	3	−2836[b]	2.21	625
33.9°N, 4.1°E	2.3	1.1	−2535[b]	1.98	499
34.1°N, 3.3°E	2	1.2	−2527[a]	3.11	322
35.8°N, 0.4°E (Figure 10)	3.5	3.6	−3683[b]	1.68	574
37.2°N, 1.65°E (basin C; Figure 2c)	0.85	0.75	−3048[b]	3.5	273

[a]Elevation estimated from MOLA shot point.
[b]Elevation estimated from gridded MOLA data.

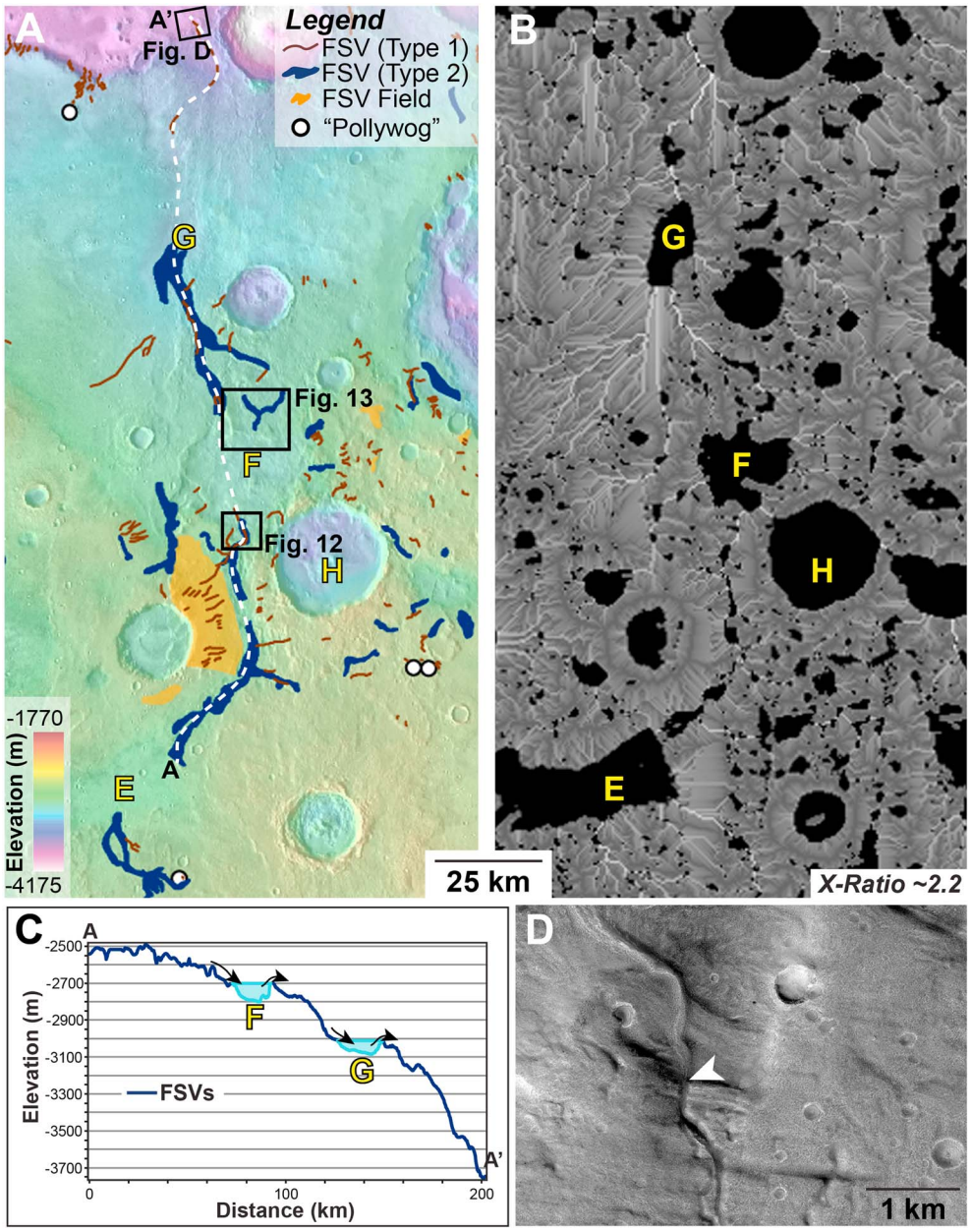

Figure 11. (a) Regional view (see Figure 4 for context) of the informally named Northern Plains valley system where three main FSV segments connect basins E, F and G to make a 200 km-long valley system (white dashed line). The depressions were likely filled with (ice-covered?) lakes and were the source of water for valley formation. Boxes show locations of Figures 12 and 13. MOLA over THEMIS Day IR. Centered near 38.2°N, 3.8°E, north to top. (b) Regional hydrologic modeling predicts location, size, and volume of filled depressions and flow paths across the landscape in the area of Figure 11a (see Figure 5 for flow path and lake explanation and Table 1). Model result equivalent to an *X* ratio of ~2.2 (see text), consistent with the point at which basin E would have overflowed into basin F, transporting sediment toward the northern plains. (c) Profile of transect in Figure 11a indicating regional gradient (0.006) toward the dichotomy boundary and location of proposed lakes that fed valley incision. FSVs are preserved in the morphology between depressions in the landscape (e.g., Lakes E, F, and G) and terminate in the northern plains. (d) The terminus of the Northern Plains valley system transitions from an incised to inverted channel along the dichotomy boundary, possibly suggesting flow continuing beneath an ice cover forming an esker. Subframe of HiRISE ESP_041144_2200 (59.8 cm scaled pixel width with illumination from upper left). North to top.

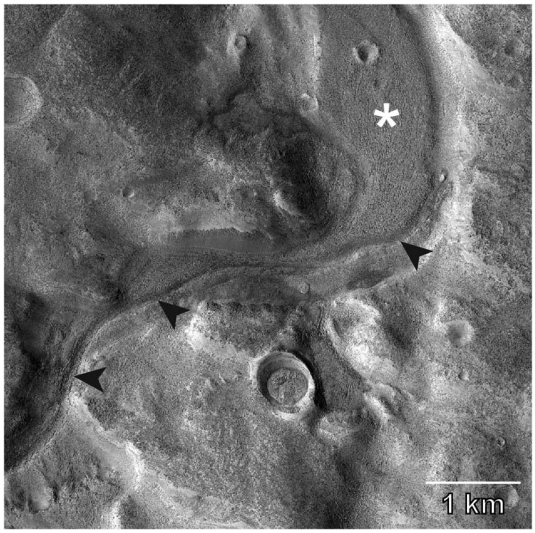

Figure 12. Northern Plains valley system showing inlet valley into basin F (see Figure 11a for context). Black arrows show narrow incised (Type 1) channel within broader (Type 2) valley as system debouches into basin G. Possible broad depositional landform at margin of basin F (asterisk sign). Subframe of HiRISE ESP_042568_2180 (29.7 cm scaled pixel width). North to top.

From the northern margin of basin F, the valley incises ~40 km with an average gradient of 0.008 before disappearing at the model predicted margin of basin G. The model-predicted volume of basin G is only 13 km^3, and the model predicts overflow would only occur for negative *X* ratio values (Table 1). The ~60 km stretch from basin G to the system terminus has the steepest gradient of the entire Northern Plains valley system, ~0.013. A few incised valley segments are preserved along this path, and the channel transitions from incised to inverted as it crosses the dichotomy boundary (Figure 11d).

4.5. Boomerang Lake Valley System

Approximately 200 km east-southeast of basin B (Figure 4), the margins of a broadly curved depression, informally named Boomerang Lake, are heavily dissected by FSVs. Boomerang Lake breached the rim of basin I to the north and deposited a prominent steep front delta (Figure 14). The overflow channel into basin I is ~14 km in length, and the width ranges from ~150 m up to 650 m near the delta front (Figure 14c). There is no evidence for an incised interior channel. The fan surface is ~1 km long from apex to toe and has a steep front with hints of layering at HiRISE scale (Figure 14d). The platform of the delta is at an elevation of −3075 m, implying basin I was filled with water to a depth of over 850 m with a corresponding *X* ratio of ~3.9 (Table 2). After the rim was incised, the hydrologic model suggests that during wet conditions (*X* ratios up to ~3.5), both Boomerang Lake and basin I had common surface elevations and a combined volume of 1350 km^3. At an *X* ratio of about 3, the two basins are barely connected and have a combined volume of roughly 900 km^3. For higher *X* ratios the basins would host separate lakes.

The overflow event from Boomerang Lake into basin I had to overcome an initially intact crater rim, suggesting Boomerang Lake had to reach a lake level near −2385 m (Table 1). This lake surface corresponds to an *X* ratio value of roughly 1.5, implying humid conditions by Mars standards [*Matsubara et al.*, 2013]. The southern margin of Boomerang Lake has an ~18 km long outlet valley that terminates in a small delta on the floor of basin J (Figure 14). The *X* ratio at which Boomerang Lake would have been connected to the outlet valley in the south is at ~1.7, comparable to the *X* ratio required to breach the rim of lake I to the north. It is unusual for lakes to have stable overflows into two distinct outlet valleys, however. One possible explanation for the double outlet valley is an impact into a shallow Boomerang Lake that could have trigged a tsunami, resulting in overflow to the north and south forming deltas into basins I and J, respectively. There are several craters on the floor of Boomerang basin, and a few have well-preserved ejecta with radial morphologies that could be considered candidates for impact into a shallow lake (e.g., a 3 km diameter crater along the eastern margin above the white arrow in Figure 14a). Evidence for corresponding wave-related overflow features elsewhere around the margin of Boomerang basin, however, is lacking.

The deepest part of Boomerang Lake has a few 4–5 km long sinuous ridges (Figure 14, see CTX B01_009892__2148) similar in morphology to those seen in Figure 10. If these ridges are analogous to eskers, which is consistent with their morphology, their presence could indicate flow beneath a thin ice cover. An inverted fluvial channel origin for the ridges cannot be definitively ruled out, however, due to the lack of topographic data on the basin floor (for example, if the ridges went uphill and downhill and did not obey regional variations in local topography, the ridges would be more analogous to eskers than inverted fluvial channels).

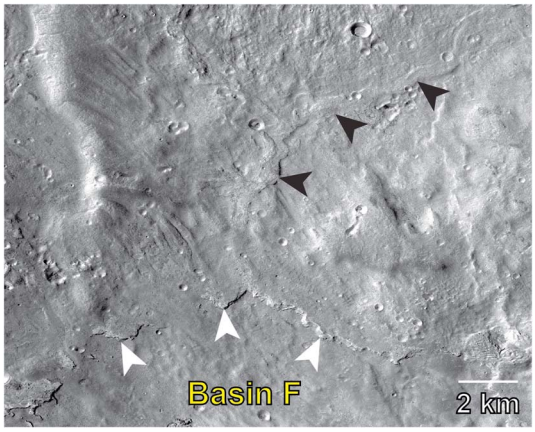

Figure 13. The inverted channels (black arrows) flowing into the northern margin of basin F (see Figure 11a for context) with associated light-toned deposits (white arrows) along the deepest part of the basin floor (−2850 m) are consist with the presence of a water-filled basin. Subframe of CTX G19_025676_2190 (6 m scaled pixel width). North to top.

5. FSV Discharge Estimates

To constrain the amount of runoff, we estimated discharge (Q) in the paleochannel of the Heart Lake FSV system (Figure 9) from hydraulic relationships estimating velocities and flow depths based upon minimum conditions required to transport bed sediment. Discharges were calculated from the morphometry and local slopes of a representative reach using HiRISE and MOLA data (Figures 9c and 9d). Discharge rates assume that active transport of bed sediment occurred, but due to the unknown nature of the channel bed, a range of possible grain sizes from medium sand ($D \sim 0.3$ mm), very coarse sand ($D \sim 2$ mm), and gravel ($D \sim 20$ cm) was considered for both the main channel and the incised channel.

The relatively straight valley segment between basin B and Heart Lake has a width and depth of ~1000 m and 70 m, respectively. The average bed width of the incised inner valley (assumed to be half of the wall-to-wall measurement) is approximately 90 m with an estimated depth of 3–10 m based on crude estimates from MOLA shot points with altimetry tracks oriented roughly perpendicular to the channel (Figures 9c and 9d). These valley depths are probably a large overestimation of the effective depth of the flow because the channels likely incised during flow events; that is, the flows probably never fully filled their valleys. Our approach using channel dimensions and estimated flow depth for sediment transport conditions representative of terrestrial rivers provides a conservative estimate of formative discharges.

Assuming medium sand bed river channels ($D \sim 0.3$ mm) and an associated Shields number τ^* of roughly 2 dyn cm^{-2}, which is representative of transport conditions being about 10 times threshold conditions in such channels [e.g., *Talling*, 2000], the effective shear stress (τ) is given by

$$\tau = \tau^*(\rho_s - \rho)g_m D$$

where sediment density (ρ_s) of basalt is approximately 3000 kg m^{-3}, fluid density (ρ) is 1000 kg m^{-3}, and adjusted Mars gravity (g_m) is 3.71 m s^{-2}. With a $\tau \sim 3.67$, the flow depth, z, can be solved by

$$\tau = \rho g z S$$

where channel gradients (S) are 0.0045 for the Heart Lake system. The calculated flow depth to transport medium sand-sized grains is ~0.26 m. The Manning equation, corrected for Martian gravity, and the channel dimensions are used to estimate discharge (Q) within the channel [after *Mangold*, 2012; *Mangold and Howard*, 2013] by

$$Q = A\left(g_m S R^{4/3}/g_e n^2\right)^{1/2}$$

where A is the cross-sectional area of the channel; S is the characteristic channel gradient (0.0045); R is the hydraulic radius (cross-sectional area divided by wetted perimeter); g_m and g_e are gravity for Mars (3.71 m s^{-2}) and Earth (9.8 m s^{-2}), respectively; and n is the Manning coefficient, assumed to be equal to 0.04.

The discharge in the main channel and incised channel for medium sand ($D \sim 0.3$ mm) is approximately 177 m^3 s^{-1} and 16 m^3 s^{-1}, respectively. This result is of the same order of magnitude as earlier estimates of discharge in FSV systems [e.g., *Adeli et al.*, 2016; *Howard and Moore*, 2011; *Parsons et al.*, 2013; *Salese et al.*, 2016]. In the Heart Lake system, the minimum timescale for the hydrologic system to fill basin B (188 km^3) from overflow of basin A based on a discharge of 16 m^3 s^{-1} (from the incised interior channel dimensions) is 372 years. Based on the width of the main channel and associated discharge of 177 m^3 s^{-1}, the minimum timescale required to fill basin B is about 35 years.

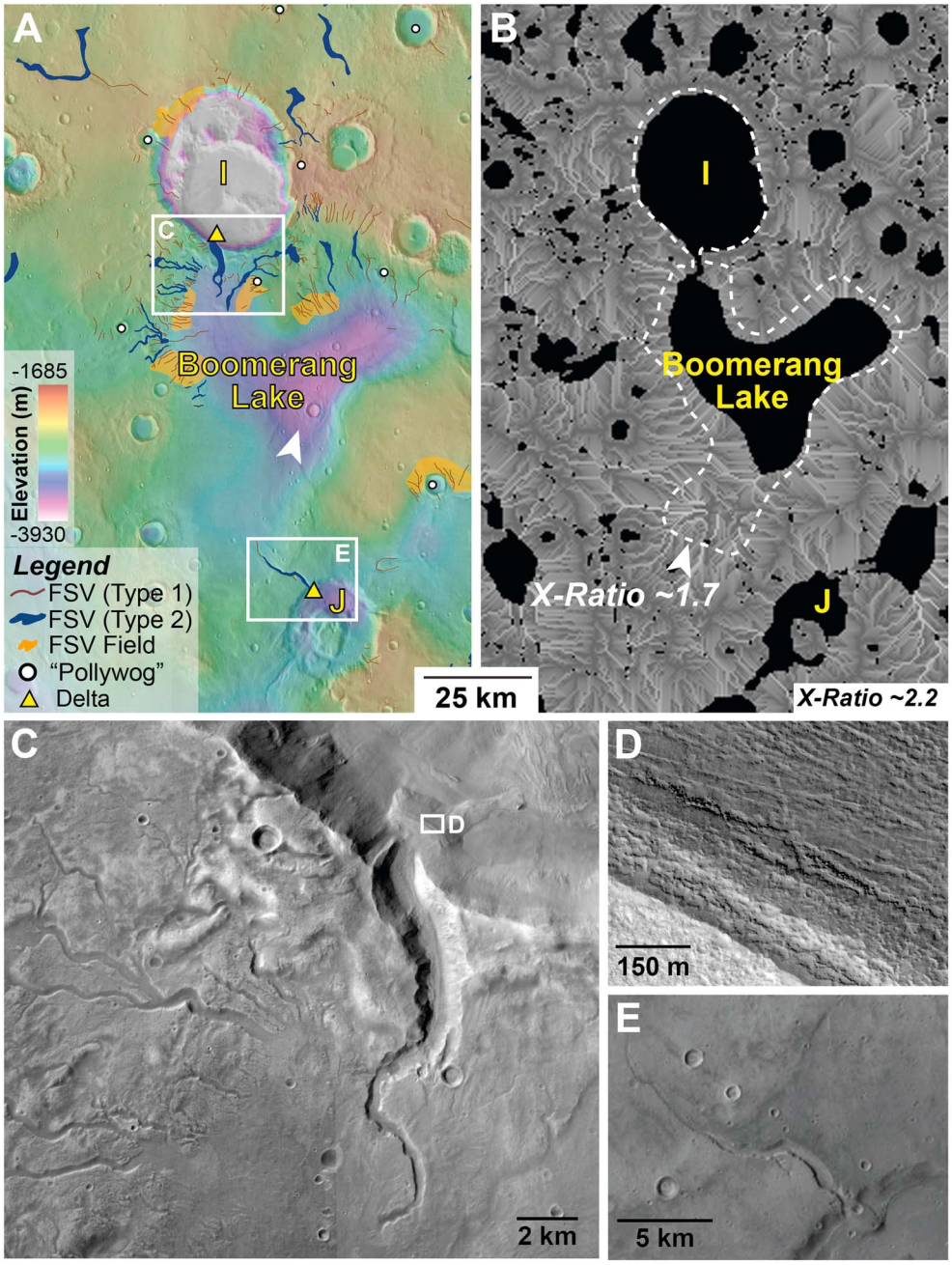

Figure 14. (a) Regional view (see Figure 4 for context) of the informally named Boomerang Lake valley system. This system has a high concentration of FSVs along the northern margin of Boomerang Lake. White boxes location of Figures 14c and 14e. Several sinuous ridges (e.g., white arrow) analogous to eskers occur on the deepest parts of the basin floor. MOLA over THEMIS Day IR. Centered near 34.4°N, 6.5°E, north to top. (b) Regional hydrologic modeling predicts location, size, and volume of filled depressions and flow paths across the landscape in the area of Figure 14a (see Figure 5 for flow path and lake explanation and Table 1). At an *X* ratio of ~2.2, basins I and Boomerang would be connected. Conditions would have to be more humid (*X* ratio ~1.7, white dashed line) for Lake Boomerang to extend far enough south to overflow along its southern margin to form small delta in basin J. (c) FSVs and lobe deposit on the floor of basin I. Subframe of CTX D08_030344_2155 (5.94 m scaled pixel width). (d) Subtle layers and blocks visible on delta front; delta surface at lower left. Subframe of HiRISE ESP_041223_2155 (29.7 cm scaled pixel width), north to top. (e) The small (~2 km long) delta in basin J created by overflow from Boomerang Lake. Subframe of CTX B01_009892_2148 (5.88 m scaled pixel width).

Discharge estimates, however, vary as a function of grain size, which is a variable that cannot be determined from orbital data. For example, a channel bed consisting of very coarse sand ($D \sim 2$ mm) would have an estimated minimum flow depth of roughly 1.7 m and associated discharges of 4178 $m^3 s^{-1}$ in the main channel and 376 $m^3 s^{-1}$ in the incised channel. In the Heart Lake system, the minimum timescale for the hydrologic system to fill basin B from overflow of basin A based on a discharge of 376 $m^3 s^{-1}$ (from the incised interior channel dimensions) is 16 years. Based on the width of the main channel and the associated discharge of 4178 $m^3 s^{-1}$, the minimum timescale required to fill basin B is about 1.5 years.

Gravel in terrestrial channels is typically transported close to threshold conditions, with $\tau^* \sim 0.06$. For coarse gravel sized grains ($D \sim 20$ cm), the minimum flow depth would be about 5 m with estimated discharges of 26,082 $m^3 s^{-1}$ in the main channel and 2347 $m^3 s^{-1}$ in the incised channel. The minimum timescale for the hydrologic system to fill basin B from overflow of basin A based on a discharge of 2347 $m^3 s^{-1}$ (from the incised interior channel dimensions) is 2.5 years. Based on the width of the main channel and the associated discharge of 26,082 $m^3 s^{-1}$, basin B would fill up in about 3 months.

6. Estimate of FSV Age From Crater Statistics

Previous studies have shown that clusters of FSVs developed on or near the fluidized ejecta of relatively well-preserved and presumably young craters [e.g., *Hobley et al*., 2014; *Mangold*, 2012; *Morgan and Head*, 2009]. The association of FSVs with young craters is not universal, however. In northern Arabia Terra, roughly 21% of Type 1 FSVs occur on well-preserved crater ejecta with the majority of FSVs forming between craters or near-degraded craters (Figure 15). In order to investigate possible relationships between ejecta and valley formation and to constrain the age of FSV formation and the timing of fluvial activity, we used crater statistics to estimate the age of craters with well-preserved ejecta that preserve a range of fluvial dissection (Figure 16).

We classified each ejecta as having a high linear density of FSVs (class 1; $n = 7$), a low linear density of FSVs (class 2; $n = 6$), or no evidence of FSVs (class 3; $n = 9$) (Figure 15 and Table 3). The linear density of class 1 ejecta ranges from 0.042 to 0.24 km^{-1} (average 0.099 km^{-1}) and the linear density of class 2 ejecta ranges from 0.007–0.054 km^{-1} (average 0.023 km^{-1}; Table 3). A plot combining the estimated crater age versus the degree of fluvial modification is shown in Figure 17. The maximum estimated model age of craters whose ejecta have a high linear density of FSVs (class 1) are all greater than ~3.5 Ga, with relative ages corresponding to the Hesperian (Figure 17 and Table 3). The maximum estimated model age of craters whose ejecta have a low linear density of FSVs (class 2) are mostly older than 3 Ga (with the exception of crater 11 that is ~2.3 Ga (+0.83/−1)) with relative ages corresponding to the Hesperian to Amazonian/Hesperian (Figure 17 and Table 3). By contrast, the majority of craters with well-preserved ejecta that are not dissected (class 3) are all less than 2.1 Ga with relative ages corresponding to the Amazonian (Figure 17 and Table 3). Crater 17 is the exception, as it has an approximate absolute age of 3.5 Ga (+0.11/−0.62) but remains fluvially unmodified. The most likely period during which FSVs formed, therefore, was during a relatively short time interval between roughly 3.5 to 2 Ga, with 3 to 3.5 Ga likely representing the oldest period during which incision began.

The cumulative curves for craters 4, 6, and 7 have an observed break in slope parallel to the expected production function (crater diameter range of 0.7–1 km) that yield estimated model ages of 3.39 Ga (+0.11/−0.36), 3.03 Ga (+0.29/−0.80), and 3.28 Ga (+0.11/−0.24), respectively (Figure 16). This putative break in slope could represent an erosional event related to the formation of the FSVs themselves, which is consistent with the range of possible ages indicated by the collection of statistics (Figure 17). This conclusion is tentative, however, because the break in slope could also be related to steady state erosion.

We recognize uncertainties introduced by using relatively small individual count areas [e.g., *Grant et al*., 2014; *Platz et al*., 2013; *Warner et al*., 2015] (Figure 16), but collectively, these statistics suggest that (1) well-preserved ejecta with a high linear density of valleys are relatively older than well-preserved ejecta that is not (or less) modified by fluvial activity and (2) most FSV formation likely occurred in a relatively short-lived event sometime around the Amazonian/Hesperian transition to approximately the middle Amazonian (Figure 17).

This data set also allows us to consider relationships between FSVs and crater variables such as size, latitude, and ejecta elevation and morphology (Table 3). The class 1 ejecta typically have lobate ejecta and more degraded crater interiors that could reflect modification by multiple processes in addition to formation of

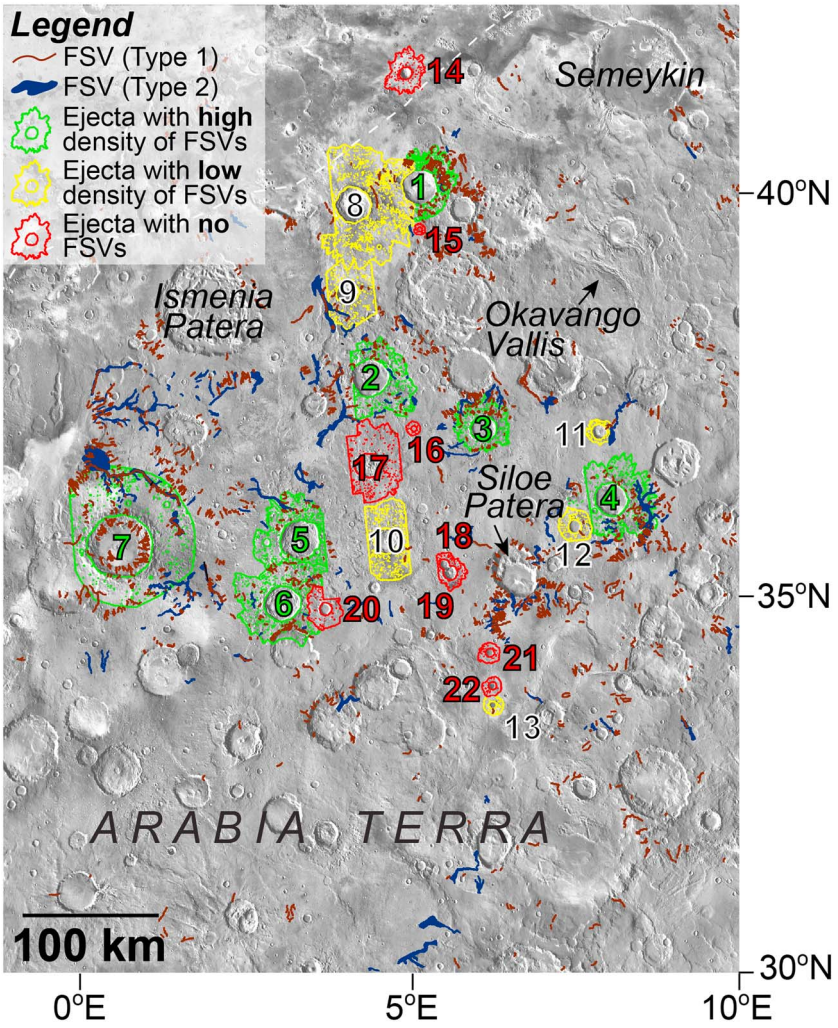

Figure 15. The majority of mapped FSVs are not associated with crater ejecta. All well-preserved ejecta deposits were mapped as having a (1) high linear density of Type 1 FSVs (Class 1, green), (2) low linear density of Type 1 FSVs (Class 2, yellow), or (3) no Type 1 FSVs (Class 3, red). Craters were counted using CTX data (some ejecta margins were mapped only to the extent of available data). White dashed line shows approximate location of the northern dichotomy boundary. See Figures 16 and 17 for the results of the crater statistics and Table 3 for characteristics of the mapped craters.

the FSVs. By contrast, class 2 and 3 ejecta have a less modified crater interior and a strong radial pattern on their ejecta. The crater age, composition of surface materials or substrate, and (or) the topography could influence the ejecta morphology. On average, class 1 ejecta are associated with larger craters (Table 3), which is expected from the impact flux that predicts a decrease in crater size population over time. The elevation of the crater ejecta and the latitude do not seem to have a significant role in the distribution of FSVs.

7. Discussion

7.1. Mechanisms for Fluvial Activity and Sources of Water

A variety of mechanisms have been proposed to account for the formation of post-Noachian valleys including hydrothermal circulation on volcanoes [*Gulick*, 2001b; *Gulick and Baker*, 1990], melting of a snowpack from volcanic heating [*Fassett and Head*, 2006, 2007], melting of ice-rich deposits due to a favorable microclimate at low relative elevations [*Dickson et al.*, 2009], glaciofluvial [*Fassett et al.*, 2010], and flow beneath thin, regionally extensive ice cover [*Hobley et al.*, 2014]. *Carr and Head* [2003] suggest that snow and ice accumulations hundreds of meters thick might melt at their base leading to discharge that excavates fluvial

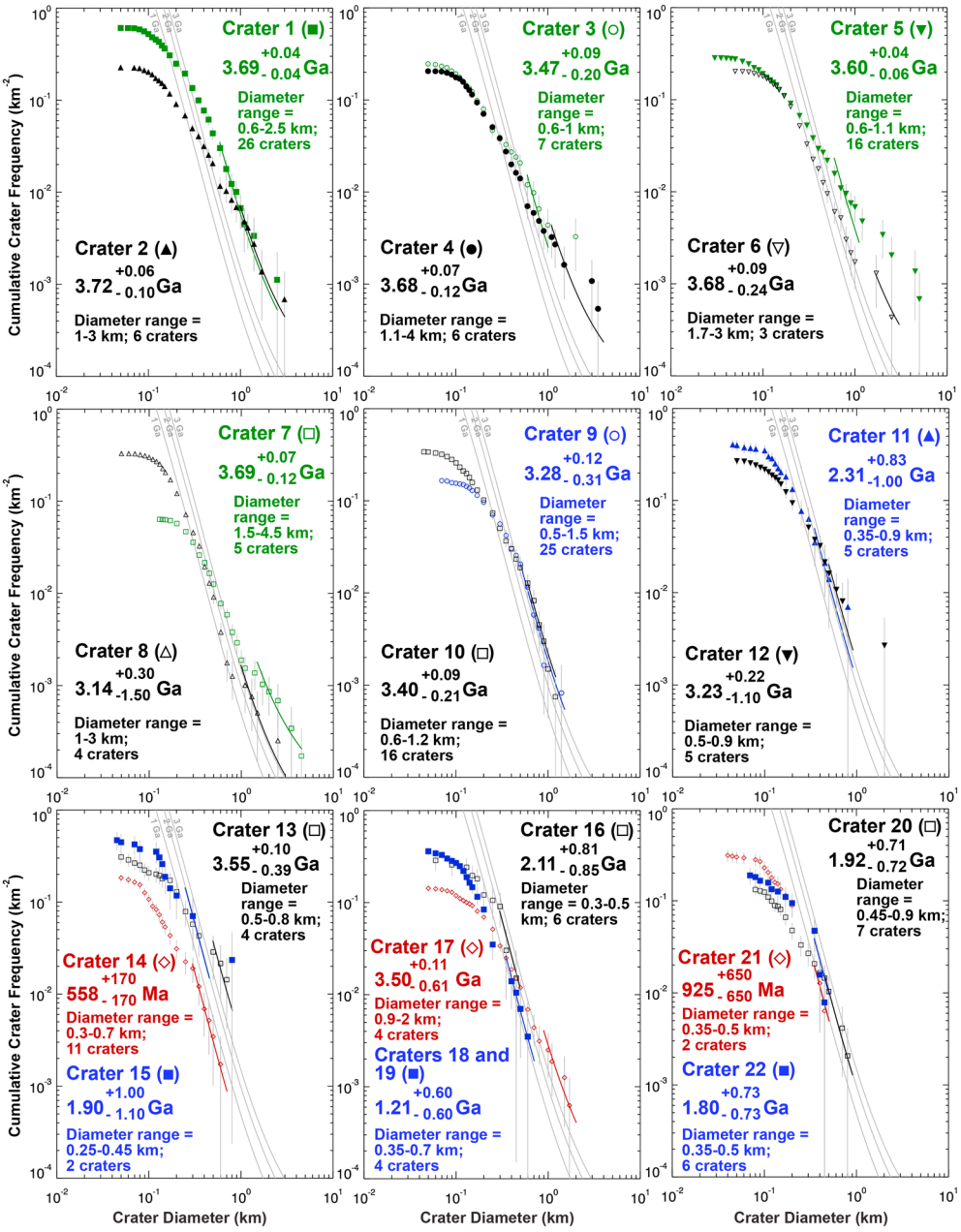

Figure 16. Cumulative crater statistics for well-preserved ejecta mapped in Figure 15 based on the chronology function from *Hartmann and Neukum* [2001] and a production function from *Ivanov* [2001]. Example absolute ages estimated using Craterstats2 algorithm (error bars reflect ± $1/N^{0.5}$) [*Michael and Neukum*, 2010] using the largest craters that provide the best fit to the expected production function (Table 3). The cumulative resurfacing correction of *Michael and Neukum* [2010] was not applied. The cumulative curves for craters 4, 6, and 7 have a break in slope parallel to the expected production function at crater diameters ranging between 700 m and 1 km that correspond to model ages of 3.39 Ga (+0.11/−0.36) based on five craters, 3.03 Ga (+0.29/−0.80) based on eight craters, and 3.28 Ga (+0.11/−0.24) based on 23 craters (see text for discussion).

channels. Other research suggests that valley formation is linked to impact cratering, either directly, such that the heat generated from the impact would melt the ice-rich subsurface beneath the ejecta [*Williams and Malin*, 2008; *Morgan and Head*, 2009; *Jones et al.*, 2011; *Mangold*, 2012; *Mangold et al.*, 2012; *Salese et al.*, 2016; *Segura et al.*, 2002, 2008; *Toon et al.*, 2010], or indirectly, where the impact would inject water vapor into atmosphere that would result in regional snow accumulation and subsequent melting [*Goddard et al.*, 2014; *Kite et al.*, 2011].

Table 3. Characteristics of Craters With Well-Preserved Ejecta in the Study Region

Ejecta Class	Label[a]	*D* (km)	Latitude (°N)	Approximate Elevation of Crater Ejecta[b] (m)	Cumulative Length of FSVs[c] on Ejecta (km)	Area (km^2)	Linear Density (km^{-1}) FSVs[c]	Ejecta Morphology	Estimated Maximum Model Age[e]	RA[f]
Class 1: High linear density of FSVs	1	25.8	40	−2975	217.8	894	0.24	lobate	3.69 Ga (+0.04/−0.04)	H
	2	27.7	37.7	−2500	69.37	1451	0.048	lobate	3.72 Ga (+0.06/−0.10)	H
	3	18.9	37.1	−2100	100.2	917	0.11	lobate	3.47 Ga (+0.09/−0.20)	H
	4	23.9	36.2	−2250	119.67	1855	0.065	lobate	3.68 Ga (+0.07/−0.12)	H
	5	29.4	35.7	−2250	61.1	1467	0.042	lobate	3.60 Ga (+0.04/−0.06)	H
	6	27	34.9	−2100	192.3	2308	0.083	lobate	3.68 Ga (+0.09/−0.24)	H
	7	48	35.6	−2475	307.8	5822	0.053	lobate	3.69 Ga (+0.07/−0.12)	H
	Avg.	28.7	36.7	−2380	152.6	2102	0.099	lobate	--	H
Class 2: Low linear density of FSVs	8	25.4	39.8	−3350	63.01	3965	0.016	radial	3.14 Ga (+0.30/−1.50)	A/H
	9	17	38.8	−2850	17.37	1215	0.014	radial	3.28 Ga (+0.12/−0.31)	A/H
	10	18.5	35.6	−2150	9.552	1335	0.0072	radial	3.40 Ga (+0.09/−0.21)	H
	11	11.5	37	−2150	7.754	143	0.054[d]	lobate	2.31 Ga (+0.83/−1.00)	A/H
	12	9.4	35.8	−2100	6.4	373	0.017	radial	3.23 Ga (+0.22/−1.10)	A/H
	13	5.7	33.6	−2220	3.8	139	0.028	radial	3.55 Ga (+0.10/−0.39)	A/H
	Avg.	14.6	36.8	−1753	17.98	1195	0.023	radial	--	A/H
Class 3: No FSVs	14	9.2	41.5	−3650	0	579	0	lobate	558 Ma (+170/−170)	A
	15	3.4	39.5	−2825	0	42	0	radial	1.90 Ga (+1.0/−1.1)	A
	16	4.1	37.1	−2100	0	66	0	radial	2.11 Ga (+0.81/−0.85)	A
	17	17.5	36.6	−2275	0	1596	0	lobate	3.5 Ga (+0.11/−0.61)	A/H
	18	7.3	35.4	−2000	0	286	0	radial	1.21 Ga (+0.60/−0.60)	A
	19	10.4	35.3	−2050	0		0	radial		
	20	9.2	34.8	−2200	0	571	0	radial	1.92 Ga (+0.71/−0.72)	A
	21	6.6	34.3	−2160	0	157	0	radial	925 Ma (+650/−650)	A
	22	5.9	33.8	−2325	0	127	0	radial	1.80 Ga (+0.73/−0.73)	A
	Avg.	8.2	36.5	−2398	0	428	0	radial	--	A

[a]See Figure 15.
[b]Relative to MOLA.
[c]Type 1 FSVs.
[d]Only one valley segment.
[e]See Figures 16 and 17.
[f]RA is "relative age" where H is "Hesperian", and "A" is Amazonian, based on estimated model ages including error bars. "D" is crater diameter.

The aforementioned studies attribute valley formation to local environmental conditions and (or) localized melting of ice from endogenic heat sources, which is not consistent with the nature and distribution of FSVs in northern Arabia Terra. Some investigations, however, suggest that valleys required at least regionally extensive precipitation, either producing direct runoff or melting of accumulated snow and ice [*Adeli et al.*, 2016; *Ansan and Mangold*, 2006; *Burr et al.*, 2010; *Howard and Moore*, 2011; *Mangold et al.*, 2004, 2008]. At present, evidence for Amazonian-Hesperian paleolakes that are contemporaneous with fluvial valley formation is limited, but previous studies include examples from Tempe Terra along the dichotomy boundary (35.6°N, 305.3°E) [*Salese et al.*, 2016], the region near Ares Vallis (0–17°N, 330–350°E) [*Warner et al.*, 2010b], Eberswalde crater (e.g., as summarized in *Irwin et al.* [2015]), and Gorgonum basin (37°S, 189°E) [*Howard and Moore*, 2011].

7.2. Evidence for Paleolakes

Regional mapping reveals that the majority of valleys occur far from young impact craters, making a direct and (or) indirect association with impact processes less probable (Figure 15). Instead, the valleys characteristically start abruptly on uplands and terminate along the flanks of numerous depressions at elevations that correspond remarkably well to model-predicted lake surfaces at an *X* ratio of ~2.2 (Figure 6). We propose some FSV segments flowed both into and out of paleolakes to form 150–200 km long valley systems. The morphological evidence supporting the continuity of FSVs across intravalley depressions such as basin B in the Heart Lake system (section 4.3) and basins F and G in the Northern Plains system (section 4.4) includes (1) consistent widths of the basin inlet and outlet, including an incised channel within a larger channel; (2) equal elevation for the termination and origin of the level of the incoming and outgoing channels, respectively; (3) absence of FSVs on the inferred paleolake floor below level of the valley inlet and outlet; (4) overall

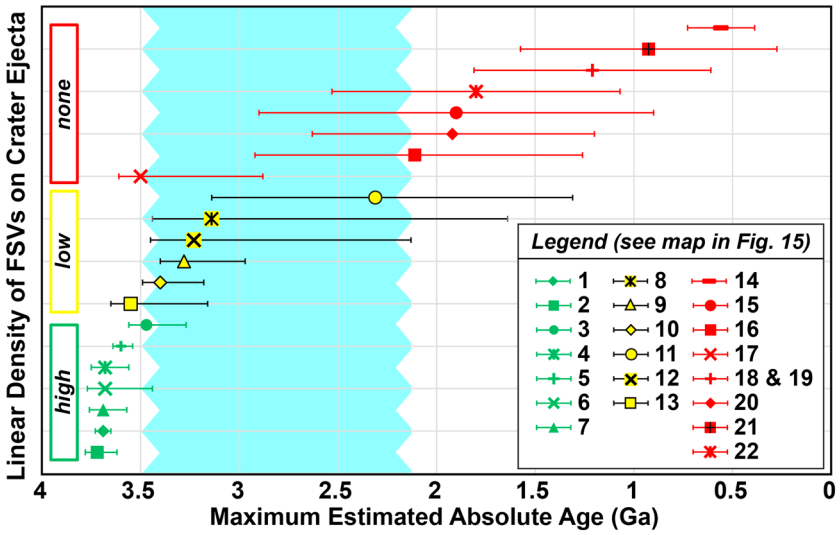

Figure 17. Maximum estimate ages of the well-preserved crater ejecta in the study region (Figure 16) categorized by their degree of fluvial dissection (Figure 15). The well-preserved ejecta with a high linear density of valleys are relatively older than well-preserved ejecta that is not (or less) modified by fluvial activity. The most likely period during which FSVs formed (blue shaded region) was during a relatively short time interval between roughly 3.5 to 2 Ga, with 3 to 3.5 Ga likely representing the oldest period during which incision began.

continuity of profile of FSV system above and below inferred lake, after accounting for the intervening flat lake surface; and (5) the modeled lake would have overflowed for the *X* ratio value that correlates best with the regional occurrence and distribution of FSVs (particularly their downstream terminations).

Morphological evidence consistent with the location and extent of the modeled paleolakes includes (1) equal elevation for the termination and origin of the level of the incoming and outgoing FSVs at the modeled margins of the basins; (2) inferred sedimentary fan deltas occur along the interior margins of some model-predicted lakes; (3) fans, if deltaic in origin, would imply deposition into deep bodies of standing water, which is consistent with the observation that the fans are located hundreds of meters above the floors of their respective host basins (Table 2); (4) some fan deltas preserve evidence of fluctuating lake levels (Figures 7d and 10); and (5) basin floor deposits inferred to be sedimentary in origin (Figures 2d and 8b) are associated with model-predicted filled basins (Figure 6).

7.3. Discharge Estimates and Style of Erosion

The wide and strongly incised channel immediately downstream from the outlet of basin B is exceptional for FSVs in the study region and is indicative of high-discharge flow (Figure 9b). This system could have formed from (1) multiple, sustained flows or (2) a single overflow event with a complex history of widening and valley incision that lead to the abandonment of depositional bars related to peak flow stages, similar to the Noachian-Hesperian Okavango Valles [*Mangold and Howard*, 2013]. The downcutting of the outflow valley (Figure 9b) supports formation by a single overflow event, but the comparable width of the basin B inlet valley (Figure 8) is more consistent with relatively high runoff throughout the entire system. If the outlet from basin B (Figure 9) experienced rapid breaching and downcutting of the lake outlet, discharge rates may have greatly exceeded the estimates stated in section 5 for a short period of time [e.g., *Mangold and Howard*, 2013].

Most of the FSVs in Arabia Terra do not have incised channels and could have formed in a single episode of erosion. The presence of incised interior channels as in the Heart Lake and Northern Plains systems, however, supports formation via progressive erosion [e.g., *Irwin et al.*, 2005b]. The interior channel could have formed as water levels decreased and the channel became entrenched, perhaps in response to a change in hydrologic regime toward increasing aridity. Alternatively, the incised channels could be related to smaller lake-overflow events that occurred subsequent to a main overflow event or as a response to changes in local base level.

Estimated discharges vary considerably as a function of grain size as well as assumptions about the nature of the flow within the channel. As discussed in section 5, discharge estimates based on the dimensions of the

incised interior channel ranges from approximately tens to hundreds to thousands of $m^3 s^{-1}$ based on the active transport of medium sand, very coarse sand, and gravel, respectively. Likewise, discharge estimates based on the dimensions of the main channel ranges from hundreds to thousands to tens of thousands of $m^3 s^{-1}$ for a medium sand, very coarse sand, and gravel bed, respectively. We calculated similar estimated discharges using empirical roughness coefficients based upon sediment size, channel gradient, Shields stress, and sediment density [e.g., *Morgan et al*., 2014]. *Mangold* [2012] estimated much higher discharge rates (500–10,000 s $m^3 s^{-1}$) for valleys on ejecta in northern Arabia Terra area based on greater flow depths using a range of estimated channel depths. We consider our discharge estimates to be conservative, and they are commensurate with runoff yields from snowmelt on Mars [e.g., *Howard and Moore*, 2011; *Kite et al*., 2013; *McKnight*, 2011; *Moore et al*., 2003; *Parsons et al*., 2013; *Salese et al*., 2016]. Terrestrial analogues would include snowmelt-fed streams at high elevation or high latitude such as in Cornwallis Island in the Canadian Arctic or the Tibetan Plateau, where valleys are characterized by low drainage densities and incised channels that serve as traps for windblown snow.

7.4. The Role of Groundwater

The formation of a thick cryosphere in the Hesperian and Amazonian makes a groundwater-related source (e.g., groundwater seeps) for the formation of valleys less likely [*Clifford et al*., 2010]. This is consistent with our observations that (1) the majority of FSVs occur well away from impact craters (Figure 15), (2) many young crater ejecta lack FSVs, and (3) the presence of long valley systems (e.g., Heart Lake and Northern Plains) are not consistent with impact-generated sources and (or) groundwater seeps. Numerous single-exit-breach craters (pollywogs) that imply overflow of a deep interior crater lake, however, may argue for connection to groundwater, which could be related to groundwater upwelling previously predicted in Arabia Terra from hydrological modeling on early Mars [*Andrews-Hanna et al*., 2010].

The overflow of pollywogs in northern Arabia Terra seems to integrate into the local FSV systems, suggesting their formation was contemporaneous. If the region experienced large accumulations of snow and ice across the landscape, eventual overflow of craters with smaller diameters may occur. Although the nature of the permafrost and the groundwater table is unknown, pollywogs may be indicative of the involvement of artesian groundwater flow filling the lakes to overflow. Seasonally unfrozen lakes in terrestrial permafrost regions develop unfrozen depressions in the permafrost (taliks) which, if the lakes are sufficiently large and the permafrost sufficiently thin, can extend to the base of the permafrost (through taliks) [e.g., *Burn*, 2002]. If there is an upward hydraulic gradient in the subpermafrost aquifer, thermal advection can enhance and maintain through taliks [*Scheidegger and Bense*, 2014]. We have noted pollywog craters elsewhere located on regional slopes [e.g., *Parsons et al*., 2013] where artesian pressures beneath the permafrost might be involved and, because of the low elevation of the northern Arabia region, might be connected to a global artesian subpermafrost aquifer [*Clifford and Parker*, 2001; *Andrews-Hanna et al*., 2010]. Pollywogs are only seen in craters with diameters between 0.6 and 13 km, perhaps suggesting that this diameter range is capable of depressing the permafrost to access groundwater via fractures along the crater floor to form seasonally ice-covered lakes. Larger, deeper craters may access the permafrost layer along the crater walls and smaller craters ($<$ ~0.5 km in diameter) have insufficient depths to access groundwater.

7.5. The Timing and Duration of Fluvial Activity and Implications for Climate

The hydrologic routing model utilized in this study provides basic insight into the flow of water across a surface based on the assumed ratio of runoff to lake evaporation. The model and resulting *X* ratio values assume that (1) precipitation (or melting) is uniform across the landscape, (2) spatial properties of the surface are uniform, and (3) the resulting lake levels correspond to a yearly average of precipitation to evaporation. Although the model provides a simplified view of the regional hydrology, it is particularly useful for predicting the level at which lake overflow would occur.

In the Heart Lake system, there is clear morphologic evidence of overflow from basins A, B, and D where the model-predicted *X* ratio values corresponding to overflow are ≤ 4, ≤ 2.25, and ≤ 4, respectively (Table 1). *X* ratios for overflow of Heart Lake and basin C corresponds to values of ≤ 2.25 and ≤ 2.75, respectively. The lack of convincing morphologic evidence for overflow from basin C along with the higher *X* ratio value predicted for overflow may indicate the hydrologic system was not in a steady state with respect to an *X* ratio value of ~2.2. The *X* ratio of 2.75 for basin C could reflect issues not accounted for by the model, such as nonuniform

precipitation or time-limited infilling of basins (such that there was not enough time or available water to infill basin C but enough to infill basin B). The surface elevation of the fan delta platform in basin C (formed by overflow of basin D) corresponds to a modeled lake level with X ratio of 3.5, which is in the range for this Heart Lake system (Table 2). In the Northern Plains system, morphologic evidence of overflow from basins E and F correspond to model-predicted X ratios of ≤ 2.5 and ≤ 4, respectively. The X ratios necessary to provide lake levels consistent with 12 within-crater deltas range from 1.4 to 3.5, averaging 2.5 (Table 2).

The degree to which we get reasonable agreement of X ratio values that are consistent with the distribution of FSVs and deltas deposited into paleolakes across the region is indicative of a relatively stable climate over the timescale that the FSVs were active. As explained by *Matsubara et al*. [2013], the value of the X ratio does not correspond to any one combination of precipitation, runoff, and evaporation—several combinations of values for these variables could result in the same X ratio. For example, an X ratio of ~2.2 could result from $P = 0.5$ m yr^{-1}, $R = 0.45$, and $E = 1$ m yr^{-1}, or $P = 1.45$ m yr^{-1}, $R = 0.17$, and $E = 2$ m yr^{-1} [after *Matsubara et al*., 2013]. In terrestrial systems with through-flowing drainage, corresponding X ratios would be in the range of -1 to 0, whereas in terrestrial deserts the X ratio may exceed 20 [*Matsubara et al*., 2013]. *Matsubara et al*. [2011] found X ratio values in the range of 3–7 for the late Noachian climate on Mars, which would be comparable to the evaporation and precipitation regime during the late Pleistocene epoch in the Great Basin region when lakes Lahontan and Bonneville were at their greatest extent [*Matsubara and Howard*, 2009].

The widespread distribution of FSVs (Figure 3), their similar morphology and modest state of degradation is consistent with formation during a global interval of favorable climate. The climate suggested by the landforms and modeling in Arabia Terra was capable of sustaining a considerable volume of water on the landscape, with basin B alone containing a volume of water greater than the present-day Lake Tahoe in California (Table 2). Given the presumed cold temperatures in Hesperian and Amazonian, it is likely that larger bodies of water remained frozen for most of the time and valleys formed during intermittent melting events. The presence of ice-covered lakes is consistent with the sinuous ridges on some basin floors that could be eskers. The proposed Hesperian-Amazonian snowmelt-based hydrology likely continued seasonally or episodically over hundreds of years although shorter time scales are possible. Lake levels are interpreted to be an average response to longer-term climate conditions.

The increased coverage of high-resolution images has facilitated the identification and analysis of post-Noachian fluvial landforms that further our understanding of the climate evolution of Mars. These landforms, including valleys in the midlatitude regions of both hemispheres [e.g., *Adeli et al*., 2016; *Dickson et al*., 2009; *Fassett and Head*, 2008, 2011; *Hauber et al*., 2013; *Howard and Moore*, 2011; *Hynek et al*., 2010; *Salese et al*., 2016; *Warner et al*., 2010a, 2010b] as well as alluvial fans at the equator to midlatitudes [e.g., *Grant and Wilson*, 2011, 2012; *Grant et al*., 2014; *Moore and Howard*, 2005; *Morgan et al*., 2014; *Wilson et al*., 2013], challenge the paradigm that fluvial activity ceased at the Noachian-Hesperian boundary. The trigger for climatic warming could be related to obliquity-driven changes in insulation [e.g., *Laskar et al*., 2004] or warming from ephemeral atmospheric changes [*Hobley et al*., 2014]. Evidence supporting the existence of an active hydrologic cycle during the Hesperian to Amazonian is intriguing, as the associated (ice-covered?) lakes may have provided habitable environments for microbial life to form and (or) persist on Mars.

8. Summary

Modification by water and ice on a paleolandscape is one of the most unambiguous markers of past climate. The widespread distribution of FSVs in the midlatitudes, their similar morphology, and modest state of degradation is consistent with most forming during a global interval of favorable climate, likely through snowmelt from surface or sub-ice flows. The distribution and morphology of the FSVs in northern Arabia Terra is consistent with an active hydrological system near the Hesperian-Amazonian boundary during a time period on Mars that was always thought to be less favorable for precipitation (in the form of snow) and runoff. The modeled paleolakes in northern Arabia Terra imply a considerable depth of water on the landscape late in Mars history, possibly extending habitable conditions well into the Amazonian. Similar FSVs occur at the equator, but they are often harder to distinguish from older valley networks, and in some cases they may reactivate older channels. The transient warming that formed FSVs in the midlatitudes may be contemporaneous with alluvial fan and delta formation in equatorial to midlatitudes.

Acknowledgments
Thanks to Cathy Quantin-Nataf and Nick Warner for their insightful reviews and to Caleb Fassett for his Associate Editor evaluation. This work was supported by a NASA grant 12-MDAP12-0033 from the Mars Data Analysis Program. The data used are listed in the figures, tables, supplemental material, and or repository at http://airandspace.si.edu/CEPSData.

References

Adeli, S., E. Hauber, M. Kleinhans, L. Le Deit, T. Platz, P. Fawdon, and R. Jaumann (2016), Amazonian-aged fluvial system and associated ice-related features in Terra Cimmeria, Mars, *Icarus*, *288*, 286, doi:10.1016/j.icarus.2016.05.020.

Andrews-Hanna, J. C., M. T. Zuber, R. E. Arvidson, and S. M. Wiseman (2010), Early Mars hydrology: Meridiani playa deposits and the sedimentary record of Arabia Terra, *J. Geophys. Res.*, *115*, E06002, doi:10.1029/2009JE003485.

Ansan, V., and N. Mangold (2006), New observations of Warrego Valles, Mars: Evidence for precipitation and surface runoff, *Planet. Space Sci.*, *54*, 219.

Berman, D. C., D. A. Crown, and L. F. I. Bleamaster (2009), Degradation of mid-latitude craters on Mars, *Icarus*, *200*, 77.

Burn, C. R. (2002), Tundra lakes and permafrost, Richards Island, western Arctic coast, Canada, *Can. J. Earth Sci.*, *39*(8), 1281, doi:10.1139/E02-035.

Burr, D. M., R. M. E. Williams, K. D. Wendell, M. Chojnacki, and J. P. Emery (2010), Inverted fluvial features in the Aeolis/Zephyria Plana region, Mars: Formation mechanism and initial paleodischarge estimates, *J. Geophys. Res.*, *115*, E07011, doi:10.1029/2009JE003496.

Carr, M. H. (2012), The fluvial history of Mars, *Philos. Trans. R. Soc. London, Ser. A*, *370*, 2193.

Carr, M. H., and J. W. Head (2003), Basal melting of snow on early Mars: A possible origin of some valley networks, *Geophys. Res. Lett.*, *30*(24), 2245, doi:10.1029/2003GL018575.

Christensen, P. R., E. Engle, S. Anwar, S. Dickenshied, D. Noss, N. Gorelick, and M. Weiss-Malik (2009), JMARS—A planetary GIS. [Available at http://adsabs.harvard.edu/abs/2009AGUFMIN22A..06C.]

Clifford, S. M., and T. J. Parker (2001), The evolution of the Martian hydrosphere: Implications for the fate of a primordial ocean and the current state of the Northern Plains, *Icarus*, *154*, 40, doi:10.1006/icar.2001.6671.

Clifford, S. M., J. Lasue, E. Heggy, J. Boisson, P. McGovern, and M. D. Max (2010), Depth of the Martian cryosphere: Revised estimates and implications for the existence and detection of subpermafrost groundwater, *J. Geophys. Res.*, *115*, E07001, doi:10.1029/2009JE003462.

Craddock, R. A., and A. D. Howard (2002), The case for precipitation on a warm, wet early Mars, *J. Geophys. Res.*, *107*(E11), 5111, doi:10.1029/2001JE001505.

Di Achille, G., and B. M. Hynek (2010), Ancient ocean on Mars supported by global distribution of deltas and valleys, *Nat. Geosci.*, *3*, 459.

Dickson, J. L., C. I. Fassett, and J. W. Head (2009), Amazonian-aged fluvial valley systems in a climatic microenvironment on Mars: Melting of ice deposits on the interior of Lyot Crater, *Geophys. Res. Lett.*, *36*, L08021, doi:10.1029/2009GL037472.

Fassett, C. I., and J. W. Head III (2006), Valleys on Hecates Tholus, Mars: Origin by basal melting of summit snowpack, *Planet. Space Sci.*, *54*, 370.

Fassett, C. I., and J. W. Head (2007), Valley formation on Martian volcanoes in the Hesperian: Evidence for melting of summit snowpack, caldera lake formation, drainage and erosion on Ceraunius Tholus, *Icarus*, *189*, 118.

Fassett, C. I., and J. W. Head (2008), Timing of Martian valley network activity: Constraints from buffered crater counting, *Icarus*, *198*, 61.

Fassett, C. I., and J. W. Head (2011), Sequence and timing of conditions on early Mars, *Icarus*, *211*, 1204.

Fassett, C. I., J. L. Dickson, J. W. Head, J. S. Levy, and D. R. Marchant (2010), Supraglacial and proglacial valleys on Amazonian Mars, *Icarus*, *208*, 86.

Goddard, K., N. H. Warner, S. Gupta, and J.-R. Kim (2014), Mechanisms and timescales of fluvial activity at Mojave and other young Martian craters, *J. Geophys. Res. Planets*, *119*, 604, doi:10.1002/2013JE004564.

Goudge, T. A., K. L. Aureli, J. W. Heaad, C. I. Fassett, and J. F. Mustard (2015), Classification and analysis of candidate impact crater-hosted closed-basin lakes on Mars, *Icarus*, *260*, 349, doi:10.1016/j.icarus.2015.07.026.

Grant, J. A. (2000), Valley formation in Margaritifer Sinus, Mars, by precipitation-recharged ground-water sapping, *Geology*, *28*(3), 223.

Grant, J. A., and S. A. Wilson (2011), Late alluvial fan formation in southern Margaritifer Terra, Mars, *Geophys. Res. Lett.*, *38*, L08201, doi:10.1029/2011GL046844.

Grant, J. A., and S. A. Wilson (2012), A possible synoptic source of water for alluvial fan formation in southern Margaritifer Terra, Mars, *Planet. Space Sci.*, *72*, 44, doi:10.1016/j.pss.2012.05.020.

Grant, J. A., S. A. Wilson, N. Mangold, F. Calef III, and J. P. Grotzinger (2014), The timing of alluvial activity in Gale crater, Mars, *Geophys. Res. Lett.*, *41*, 1142, doi:10.1002/2013GL058909.

Gulick, V. C. (2001a), Some ground water considerations regarding the formation of small Martian gullies, *Lunar and Planet. Sci. Conf.*, Abstract 2193.

Gulick, V. C. (2001b), Origin of the valley networks on Mars: A hydrological perspective, *Geomorphology*, *37*, 241.

Gulick, V. C., and V. R. Baker (1990), Origin and evolution of valleys on Martian volcanoes, *J. Geophys. Res.*, *95*, 14,325, doi:10.1029/JB095iB09p14325.

Hartmann, W. K. (2005), Martian cratering 8: Isochron refinement and the chronology of Mars, *Icarus*, *174*, 294.

Hartmann, W. K., and G. Neukum (2001), Cratering chronology and the evolution of Mars, *Space Sci. Rev.*, *96*, 165.

Hauber, E., T. Platz, D. Reiss, L. Le Deit, M. G. Kleinhans, W. A. Marra, T. de Haas, and P. Carbonneau (2013), Asynchronous formation of Hesperian and Amazonian-aged deltas on Mars and implications for climate, *J. Geophys. Res. Planets*, *118*, 1529–1544, doi:10.1002/jgre.20107.

Head, J. W., et al. (2003), Tropical to mid-latitude snow and ice accumulation, flow and glaciation on Mars, *Nature*, *434*, 346, doi:10.1038/nature03359.

Hobley, D. E. J., A. D. Howard, and J. M. Moore (2014), Fresh shallow valleys in the Martian midlatitudes as features formed by meltwater flow beneath ice, *J. Geophys. Res. Planets*, *119*, 128–153, doi:10.1002/2013JE004396.

Howard, A. D., and J. M. Moore (2011), Late Hesperian to early Amazonian midlatitude Martian valleys: Evidence from Newton and Gorgonum basins, *J. Geophys. Res.*, *116*, E05003, doi:10.1029/2010JE003782.

Howard, A. D., J. M. Moore, and R. P. Irwin III (2005), An intense terminal epoch of widespread fluvial activity on early Mars: 1. Valley network incision and associated deposits, *J. Geophys. Res.*, *110*, D12S14, doi:10.1029/2005JE002459.

Howard, A. D., J. M. Moore, and S. A. Wilson (2014), Fresh Shallow Valleys (FSVs) on Mars, 8th Mars conference, Pasadena, Calif., 14-18 July.

Hynek, B. M., and R. J. Phillips (2001), Evidence for extensive denudation of the Martian highlands, *Geology*, *29*(5), 407.

Hynek, B. M., and R. J. Phillips (2003), New data reveal mature, integrated drainage systems on Mars indicative of past precipitation, *Geology*, *31*(9), 757.

Hynek, B. M., M. Beach, and M. R. T. Hoke (2010), Updated global map of Martian valley networks and implications for climate and hydrologic processes, *J. Geophys. Res.*, *115*, E09008, doi:10.1029/2009JE003548.

Irwin, R. P., III, and A. D. Howard (2002), Drainage basin evolution in Noachian Terra Cimmeria, Mars, *J. Geophys. Res.*, *107*(E7), 5056, 10.1029/2001JE001818.

Irwin, R. P., III, A. D. Howard, R. A. Craddock, and J. M. Moore (2005a), An 1072 intense terminal epoch of widespread fluvial activity on early Mars: 2. Increased runoff and paleolake development, *J. Geophys. Res.*, *110*, E12S15, doi:10.1029/2005JE002460.

Irwin, R. P., III, R. A. Craddock, and A. D. Howard (2005b), Interior channels in Martian valley networks: Discharge and runoff production, *Geology*, *33*, 489.

Irwin, R. P., III, K. W. Lewis, A. D. Howard, and J. A. Grant (2015), Paleohydrology of Eberswalde crater, Mars, *Geomorphology*, *240*, 83.
Ivanov, B. A. (2001), Mars/Moon cratering ratio estimates, *Space Sci. Rev.*, *96*, 87.
Jones, A. P., A. S. McEwen, L. L. Tornabene, V. R. Baker, H. J. Melosh, and D. C. Berman (2011), A geomorphic analysis of Hale crater, Mars: The effects of inpact into ice-rich crust, *Icarus*, *211*, 259.
Kite, E. S., T. I. Michaels, S. Rafkin, M. Manga, and W. E. Dietrich (2011), Localized precipitation and runoff on Mars, *J. Geophys. Res.*, *116*, E07002, doi:10.1029/2010JE003783.
Kite, E. S., I. Halevy, M. A. Kahre, M. J. Wolff, and M. Manga (2013), Seasonal melting and the formation of sedimentary rocks on Mars, with predictions for the Gale Crater mound, *Icarus*, *223*, 181.
Kneissl, T., S. van Gasselt, and G. Neukum (2011), Map-projection-independent crater size-frequency determination in GIS environments—New software tool for ArcGIS, *Planet. Space Sci.*, *59*, 1243, doi:10.1016/j.pss.2010.03.015.
Laskar, J., A. C. M. Correia, M. Gastineau, F. Joutel, B. Levrard, and P. Robutel (2004), Long term evolution and chaotic diffusion of the insolation quantities of Mars, *Icarus*, *170*(2), 343, doi:10.1016/J.Icarus.2004.04.005.
Luo, W., and T. F. Stepinski (2009), Computer-generated global map of valley networks on Mars, *J. Geophys. Res.*, *114*, E11010, doi:10.1029/2009JE003357.
Malin, M. C., and K. S. Edgett (2000), Evidence for recent groundwater seepage and surface runoff on Mars, *Science*, *288*, 2330.
Malin, M. C., et al. (2007), Context Camera Investigation on board the Mars Reconnaissance Orbiter, *J. Geophys. Res.*, *112*, E05S04, doi:10.1029/2006JE002808.
Mangold, N. (2012), Fluvial landforms on fresh impact ejecta on Mars, *Planet. Space Sci.*, *62*, 69.
Mangold, N., and A. D. Howard (2013), Outflow channels with deltaic deposits in Ismenius Lucas, Mars, *Icarus*, *226*, 385, doi:10.1016/j.icarus.2013.05.040.
Mangold, N., C. Quantin, V. Ansan, C. Delacourt, and P. Allemand (2004), Evidence for precipitation on Mars from dendritic valleys in the Valles Marineris area, *Science*, *305*, 78.
Mangold, N., V. Ansan, P. Masson, C. Quantin, and G. Neukum (2008), Geomorphic study of fluvial landforms on the northern Valles Marineris plateau, *J. Geophys. Res.*, *113*, E08009, doi:10.1029/2007JE002985.
Mangold, N., E. S. Kite, M. G. Kleinhans, H. Newsom, V. Ansan, E. Hauber, E. Kraal, C. Quantin, and K. Tanaka (2012), The origin and timing of fluvial activity at Eberswalde crater, Mars, *Icarus*, *220*, 530.
Matsubara, Y., and A. D. Howard (2009), A spatially-explicit model of runoff, evaporation and lake extent: Application to modern and late Pleistocene lakes in the Great Basin region, western United States, *Water Resour. Res.*, *45*, W06425, doi:10.1029/2007WR005953.
Matsubara, Y., A. D. Howard, and S. A. Drummond (2011), Hydrology of early Mars: Lake basins, *J. Geophys. Res.*, *116*, E04001, doi:10.1029/2010JE003739.
Matsubara, Y., A. D. Howard, and J. P. Gochenour (2013), Hydrology of early Mars: Valley network incision, *J. Geophys. Res. Planets*, *118*, 1365, doi:10.1002/jgre.20081.
McEwen, A. S., et al. (2007), Mars Reconnaissance Orbiter's High Resolution Imaging Science Experiment (HiRISE), *J. Geophys. Res.*, *112*, E05S02, doi:10.1029/2005JE002605.
McKnight, D. (2011), Onyx River at Vanda gauge measurements. National Science Foundation McMurdo Dry Valleys Long Term Ecological Research Signature Datasets. knb-lter-mcm.9022.4.
Michael, G. G., and G. Neukum (2010), Planetary surface dating from crater size-frequency distribution measurements: Partial resurfacing events and statistical age uncertainty, *Earth Planet. Sci. Lett.*, doi:10.1016/j.epsl.2009.12.041.
Michalski, J. R., and J. E. Bleacher (2013), Supervolcanoes within an ancient volcanic province in Arabia Terra, Mars, *Nature*, *502*, 47, doi:10.1038/nature12482.
Moore, J. M., and A. D. Howard (2005), Large alluvial fans on Mars, *J. Geophys. Res.*, *110*, E04005, doi:10.1029/2004JE002352.
Moore, J. M., A. D. Howard, W. E. Dietrich, and P. M. Schenk (2003), Martian layered fluvial deposits: Implications for Noachian climate scenarios, *Geophys. Res. Lett.*, *30*(24), 2292, doi:10.1029/2003GL01900.
Morgan, A. M., A. D. Howard, D. E. J. Hobley, J. M. Moore, W. E. Dietrich, R. M. E. Williams, D. M. Burr, J. A. Grant, S. A. Wilson, and Y. Matsubara (2014), Sedimentology and climatic environment of alluvial fans in the Martian Saheki crater and a comparison with terrestrial fans in the Atacama Desert, *Icarus*, *229*, 131.
Morgan, G. A., and J. W. Head (2009), Sinton crater, Mars: Evidence for impact into a plateau icefield and melting to produce valley networks at the Hesperian-Amazonian boundary, *Icarus*, *202*, 39.
Mustard, J. F., C. D. Cooper, and M. K. Rifkin (2001), Evidence for recent climate change on Mars from the identification of youthful near-surface ground ice, *Nature*, *412*, 4111.
Neukum, G., R. Jaumann, and the HRSC Co-Investigator and Experiment Team (2004), HRSC: The high resolution stereo camera of Mars Express, *ESA Spec. Publ.*, *1240*, 1.
Palucis, M. C., W. E. Dietrich, A. G. Hayes, R. M. E. Williams, S. Gupta, N. Mangold, H. Newsom, C. Hardgrove, F. Calef III, and D. Y. Sumner (2014), The origin and evolution of the Peace Vallis fan system that drains to the *Curiosity* landing area, Gale crater, Mars, *J. Geophys. Res. Planets*, *119*, 705–728, doi:10.1002/2013JE004583.
Parsons, R. A., J. M. Moore, and A. D. Howard (2013), Evidence for a short period of hydrologic activity in Newton crater, Mars, near the Hesperian-Amazonian transition, *J. Geophys. Res. Planets*, *118*, 1082–1093, doi:10.1002/jgre.20088.
Platz, T., G. Michael, K. L. Tanaka, J. A. Skinner Jr., and C. M. Fortezzo (2013), Crater-based dating of geological units on Mars: Methods and application for the new global geological map, *Icarus*, *225*(1), 806, doi:10.1016/j.icarus.2013.04.021.
Salese, F., G. Di Achille, A. Neesemann, G. G. Ori, and E. Hauber (2016), Hydrological and sedimentary analyses of well-preserved paleofluvial-paleolacustrine systems at Moa Valles, Mars, *J. Geophys. Res. Planets*, *121*, 194–232, doi:10.1002/2015JE004891.
Scheidegger, J. M., and V. F. Bense (2014), Impacts of glacially recharged groundwater flow systems on talik evolution, *J. Geophys. Res. Earth Surf.*, *119*, 758–778, doi:10.1002/2013JF002894.
Segura, T. L., O. B. Toon, A. Colaprete, and K. Zahnle (2002), Environmental effects of large impacts on Mars, *Science*, *298*(5600), 1977, doi:10.1126/science.1073586.
Segura, T. L., O. B. Toon, and A. Colaprete (2008), Modeling the environmental effects of moderate-sized impacts on Mars, *J. Geophys. Res.*, *113*, E11007, doi:10.1029/2008JE003147.
Smith, D. E., et al. (1999), The global topography of Mars and implications for surface evolution, *Science*, *284*, 1495.
Soderblom, L. A., T. J. Kreidler, and H. Masursky (1973), Latitudinal distribution of a debris mantle on the Martian surface, *J. Geophys. Res.*, *78*(20), 4117–4122, doi:10.1029/JB078i020p04117.
Talling, P. J. (2000), Self-organization of river networks to threshold states, *Water Resour. Res.*, *36*(4), 1119, doi:10.1029/1999WR900339.

Tanaka, K. L., J. A. Skinner Jr., J. M. Dohm, R. P. Irwin III, E. J. Kolb, C. M. Fortezzo, T. Platz, G. G. Michael, and T. M. Hare (2014), Geologic map of Mars: U.S. Geological Survey Scientific Investigations Map 3292, scale 1:20,000,000, pamphlet 43 p. [Available at 10.3133/sim3292.]

Toon, O. B., T. L. Segura, and K. Zahnle (2010), The formation of Martian river valleys by impacts, *Annu. Rev. Earth Planet. Sci.*, *38*, 303, doi:10.1146/Annurev-Earth-040809-152354.

Warner, N., S. Gupta, S.-Y. Lin, J.-R. Kim, J.-P. Muller, and J. Morley (2010a), Late Noachian to Hesperian climate change on Mars: Evidence of episodic warming from transient crater lakes near Ares Vallis, *J. Geophys. Res.*, *115*, E06013, doi:10.1029/2009JE003522.

Warner, N., S. Gupta, J.-R. Kim, S.-Y. Lin, and J.-P. Muller (2010b), Hesperian equatorial thermokarst lakes in Ares Vallis as evidence for transient warm conditions on Mars, *Geology*, *38*(1), 71, doi:10.1130/G30579.1.

Warner, N. S., S. Guputa, F. Calef, P. Grindrod, N. Boll, and K. Goddard (2015), Minimum effective area for high resolution crater counting of Martian terrains, *Icarus*, *245*, 198, doi:10.1016/j.icarus.2014.09.024.

Williams, R. M. E., and M. C. Malin (2008), Sub-kilometer fans in Mojave Crater, Mars, *Icarus*, *198*, 365.

Willmes, M., D. Reiss, H. Hiesinger, and M. Zanetti (2011), Surface age of the ice-dust mantle deposit in Malea Planum, Mars, *Planet. Space Sci.*, doi:10.1016/j.pss.2011.08.006.

Wilson, S. A., J. A. Grant, and A. D. Howard (2013), Inventory of equatorial alluvial fans and deltas on Mars, *Lunar and Planet. Sci. Conf.*, Abstract 2710.